Department of Physics and Astronomy
University of Heidelberg

Bachelor Thesis in Physics
submitted by

Vincent C. Mader

born in Ulm (Germany)

February 2020

Gas accretion onto eccentric planets

This Bachelor Thesis has been carried out by Vincent C. Mader at the
Max Planck Institute for Astronomy in Heidelberg
under the supervision of
Dr. Bertram Bitsch

Abstract

When trying to study the processes involved in planet formation utilizing algorithms of computational fluid dynamics, it is often necessary to explicitly specify a model for the accretion rate of gas onto a planet. Various methods for this exist, but often it is assumed that the accretion rate can be calculated without taking the planet's orbital eccentricity into account (e.g. Ida et al. 2018, Benz et al. 2014 and Mordasini et al. 2012).

In this thesis, a simplified model of a proto-planetary disk is created using the *FARGO2D1D* algorithm, with which studies of various disk and planet parameters are made. The goal of this work is to show that the orbital eccentricity can play a large role in the accretion rate of disk material onto a planet. This is due to the fact that planets on eccentric orbits form much broader gaps in the disk via the exchange of angular momentum than would be the case for a planet on a circular orbit. These gaps are accordingly more shallow, leading to a higher gas density in the planet's Hill sphere and therefore faster accretion.

Eccentric orbits of giant planets can be generated by two ways: either by massive planets that interact with their disk or by gravitational interactions between several planets during the gas phase. This study shows that if either is the case, planets on eccentric orbits can accrete gas faster than planets on circular orbits due to the less depleted planetary gap. Future studies, especially N-body simulations where eccentricities can already arise during the gas phase, need to take these effects into account.

Zusammenfassung

Bei der Modellierung von protoplanetaren Scheiben werden häufig numerische Algorithmen verwendet, um die zur Entstehung von Planeten beitragenden Prozesse zu simulieren. Hierzu ist es notwendig, eine Akkretionsroutine zu formulieren, die die Ansammlung von Gas auf Planeten in der Scheibe beschreibt. Herkömmlicherweise wird die Akkretionsrate meist unabhängig von der Exzentrizität des Planetenorbits berechnet (e.g. Ida et al. 2018, Benz et al. 2014 and Mordasini et al. 2012). .

In dieser Bachelorarbeit wird ein vereinfachtes Modell einer protoplanetaren Scheibe mithilfe des *FARGO2D1D*-Codes aufgebaut, mit dem Studien zu verschiedenen Parametern von Scheibe und Planeten durchgeführt werden. Ziel ist es zu zeigen, dass die Exzentrizität des Orbits eine große Rolle für die Gas-Akkretionsrate auf einen Planeten spielen kann. Dies liegt daran, dass exzentrische Planeten durch den Austausch von Drehimpuls mit der Scheibe eine deutlich breitere Lücke erzeugen, als es bei einem zirkulären Orbit der Fall wäre. Diese Lücke in der Scheibe ist dementprechend weniger tief, was zur Folge hat, dass die Gasdichte innerhalb der Hill-Sphäre des Planeten deutlich höher ist. Der Planet hat somit mehr Material in seiner direkten Umgebung und die Akkretionsrate steigt an.

Planeten auf elliptischen Orbits erhalten ihre Exzentrizität meist auf eine von zwei Arten: entweder, wenn der Planet massiv genug ist, durch Interaktion mit der Scheibe oder durch gravitative Wechselwirkung zwischen mehreren Planeten während der Gas-Phase. In beiden Fällen kann ein solcher Planet deutlich schneller akkretieren als ein Planet auf einem zirkulären Orbit. Zukünftige Studien sollten dies berücksichtigen, insbesondere bei N-body-Simulationen, bei denen die Exzentrizität schon während der Gas-Phase auftreten kann.

Acknowledgements

I wish to express my deepest gratitude to Dr. Bertram Bitsch for giving me the opportunity of writing my bachelor's thesis under his supervision at the Max Planck Institute for Astronomy. I am very grateful to him for always being available with helpful answers to the questions and problems facing me during the writing of this work.

I want to thank Camille Bergez-Casalou as well, who quite a few times helped me out with friendly advice when it came to the intricacies of the FARGO2D1D code or the usage of the computer cluster.

Also, I am very grateful to Prof. Dr. Kees Dullemond for taking on the task of acting as second examiner, as well as Dr. Coryn Bailer-Jones, for inspiring me during a seminar to write my bachelor's thesis at the MPIA and for helping me establish contact with Bertram. In general, I wish to express my gratitude to Ruperto Carola University and to the MPIA Heidelberg, for the knowledge and opportunities they granted me.

Lastly, I wish to thank my mother for making it possible for me to study physics in Heidelberg, as well as my father and grandmother, who from an early age on inspired me to be curious about the universe.

Contents

List of Figures

List of Tables

Chapter 1

Introduction

1.1 Historical Context

As early as the time of the ancient Babylonian civilization, several bright objects could be distinguished from the rest of the the night sky. In contrast to the stars, which on human timescales constitute a relatively static background, these objects seemed to exhibit independent motion across the sky. This explains why the word we use today to describe these objects is *planet*, which has its origin in the ancient Greek *planetes*, literally meaning "wanderer". It was observed that every now and then, the movement of these sources of light seemed to stop and then reverse for a while. Nowadays, we of course know that this behavior is explained by the planets' independent motion around the Sun. Although it was suggested that the Earth does not make up the center of the universe relatively early, e.g. by Aristarchus of Samos in the third century B.C.E., this was not a widely accepted fact until relatively recent times.

Up until the Renaissance, the widespread world view followed a model most notably suggested by the Greek polymath Ptolemy, who argued for a geocentric universe, where the Sun, planets and stars all orbit the Earth. Each of the orbiting planets was thought to additionally travel on a so-called epicycle, which helped explain the fact that the observed planets did not always travel in the same direction in the sky as seen from Earth.

Due to their low apparent magnitudes, the planets Mercury, Venus, Mars, Jupiter and Saturn can be observed from Earth with the naked eye. Thus, they were known to most historic societies with any interest in astronomy. Not being able to explain their origin, humans in civilizations all over the world tried to give these mysterious sources of light meaning by incorporating them into their stories, mythologies and religions.

It would take almost two millenia before the heliocentric model of the solar system gained widespread attention. In the 16th century, the Polish polymath Nicolaus Copernicus formulated a model of the universe with the Sun at its center and the planets traveling around it on concentric circles. Eventually, the observations of Mars' orbit done by Johannes Kepler and his mentor Tycho Brahe lead to a new empirical description of the motions of astronomical bodies that improved on the model of Copernicus, known to us today as Kepler's laws. Among other things, Kepler realized that the planets move around the sun not on circles, but on ellipses, with the Sun positioned at one of the foci.

These observations would lead Isaac Newton to formulate his theory of gravity together with his laws of motion which, it could be argued, marked the start of the scientific revolution that would take place in the following centuries. He recognized that a simple inverse square law suffices to predict the motions of the astronomical bodies in a relatively accurate way. Additionally, he noticed that this same law held true not only for the planets, but also for any falling object here on Earth.

The new heliocentric world view provided a lot of new questions in need of answers during the following centuries. Are all stars actually suns like our own, only much farther away? Could there be planets orbiting those stars and could those planets look like our own home planet, possibly even with their own unique life forms and evolutionary histories?

An attempt to explain the origin of the Solar System was made in the 18th century in part by Immanuel Kant and Pierre-Simon Laplace in their *nebular hypothesis*, in which they argued for the former existence of a giant gas cloud. Slowly rotating, this cloud was suspected to have collapsed and subsequently flattened out due to its own gravitaty. Later on, the Sun and the planets were thought to have emerged from the gas.

After the invention of the first (semi-)modern telescopes by Galileo and Newton, the following centuries saw the discoveries of more planets in our own solar system. First Uranus in the late 1700s, then Neptune a century later, bringing the number of known planets in our solary system to eight. The discovery of Pluto and later many other objects of the same size in the outer solar system prompted the *International Astronomical Union* to formally define the term *planet* in 2006 [18]. For any object in the Solar System to be classified as a planet, it has to

1. be in direct orbit around the Sun
2. possess a mass large enough to assume a nearly round shape due to self-gravitation
3. have cleared its orbit of any larger or similarly-sized bodies

With continuing scientific and technological progress, telescope resolution improved drastically, increasing the distance at which astronomical bodies could be observed. Larger and more accurate telescopes, as well as the eventual possibility of launching these telescopes into orbit made the discovery of extrasolar planets feasible. The first discovery of such an exoplanet was confirmed by Wolszczan and Frail (1992) with about 5000 having been observed since then, most notably by the *Kepler Space Telescope*, with which alone about 2600 planets could be detected. The first direct observation of a nascent proto-planet inside a proto-planetary disk was reported in 2018, after the exoplanet *PDS 70b* was imaged using ESO's *Very Large Telescope* (Keppler et al., 2018).

These recent observations show that planets are very abundant. There might be more stars with an own planetary system than without, as has been stated in a 2018 article by NASA [33]. Observations by e.g. Petigura, Howard, and Marcy (2013) indicate that a significant portion of stars is accompanied by Earth-sized planets inside the Goldilocks zone, where liquid water can exist in a stable form and therefore one of the basic requirements for life is fulfilled. Extrapolating from these observations, it is possible that there could up to 40 billion Earth-like planets in the Milky Way alone.

The mass of observed planets ranges from about twice that of the Moon to about 30 times that of Jupiter [1], thus spanning multiple orders of magnitude. Planetary compositions depend largely on their size. Most modern planetary formation theories assume an initial buildup of a central rocky core. From there the planet evolves either into an Earth-like terrestrial planet or into a gaseous giant similar to Jupiter (Pollack et al., 1996 and Kley, W., 1999).

The processes underlying planet formation are yet to be fully explained. Accurate modeling requires an understanding of many different aspects of the natural sciences, including but not limited to magneto-hydro-dynamics, chemistry, gravity (N-body-dynamics), thermodynamics, radiative transfer and coagulation physics. Due to temporal constraints and the complexity of the topic, this bachelor's thesis can only cover a small portion of what there is to be said about this active field of study.

[1] Deuterium burning starts at about 13 Jupiter masses, making these larger objects brown dwarfs.

1.2 Proto-Planetary Disks

The current scientific consensus on the origin theory of stars and planets is based on the nebular hypothesis, which states that proto-planetary disks form when large interstellar clouds of molecular gas collapse under their own gravity (Woolfson, 1993). The chemical composition of these disks is dominated by the contribution of H_2, which in most cases makes up about 98% of the disk by mass. Besides that, there are also small quantities of helium, lithium and trace amounts of heavier elements. In observed disks, most of the matter is present in the form of gas, but some of it also exists as dust. The exact ratio of dust to gas and the distribution of these two components throughout the disk is still largely unknown (Birnstiel, Dullemond, and Brauer, 2010 and Soon et al., 2019).

The collapse of such a cloud leads to a drastic increase of gas density, pressure and temperature at its center, which for high mass clouds results in the formation of a star. Conforming to the law of momentum conservation, the cloud's angular velocity increases during the collapse. Also, the initially present statistical distribution of velocities averages out in favor of the clouds's net angular momentum. The centrifugal force present in a rotating reference frame can only balance out the pull of gravity along the radial axis. Therefore, the cloud flattens out into a disk much more wide than thick, supported only by gas pressure along the axis orthogonal to the disk. Typical disk radii are on the order of a few 100 AU (Pfalzner et al., 2015).

The flattened cloud can also be regarded as an accretion disk around the central star, which after an initial accretion phase makes up almost all ($> 99\,\%$) of the mass in the disk. Planets form from the remaining gas and dust in orbit around the star. Figure 1.1 shows two images of proto-planetary disks that were observed at the *Atacama Large Millimeter/submillimeter Array* (ALMA). The images show the thermal emission of millimeter-sized grains. Multiple circular dark regions can be seen, which could be caused by planets that push the dust particles aside due to the influence of the planet's gravity on the disk structure. (e.g. Paardekooper and Mellema, 2006).

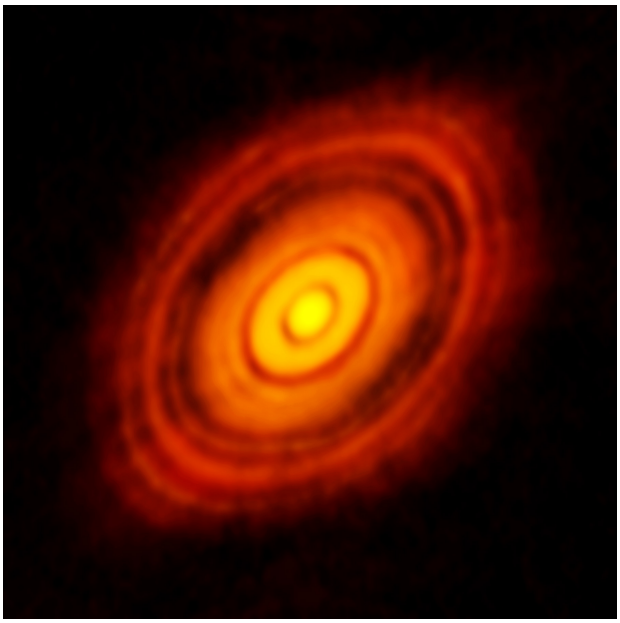

(a) Disk around *HL Tau* [1]

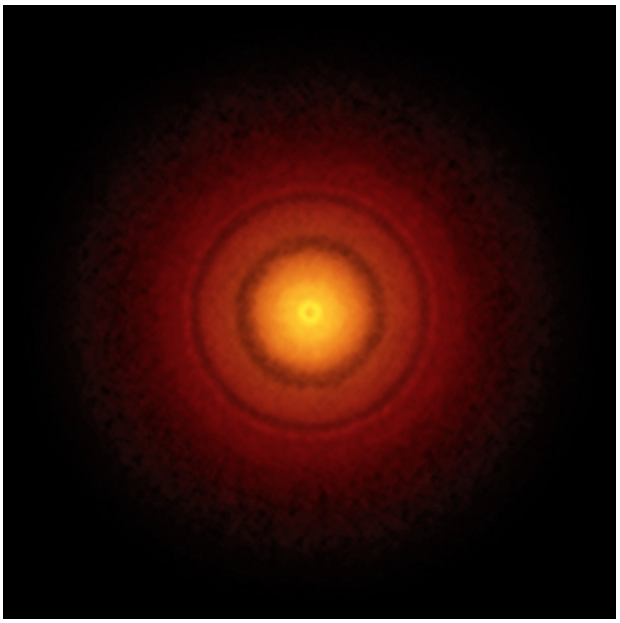

(b) Disk around *TW Hydrae* [2]

Figure 1.1: Proto-planetary disks around the stars *HL Tau* and *TW Hydrae*, observed at submillimeter wavelengths at *ALMA*. The dark rings indicate regions of lower gas density, hinting at the existence of exoplanets.

To construct a simplified model of a proto-planetary disk in two dimensions, we use cylindrical coordinates (r, φ, z). In this model, the disk is situated at $z = 0$ and is infinitesimally thin. Since observations show proto-planetary disks to be much more wide than thick anyways, this assumption makes it possible to obtain a relatively accurate, yet much less computationally constraining model. It allows us to ignore the z-dependence of the parameters describing the disk, including gas density, temperature and rotational velocity. Going from a 3D model to a 2D model in this way naturally suggests the definition of a surface density

$$\Sigma(r,t) = \int_{-\infty}^{\infty} \rho(z,t) \cdot dz \tag{1.1}$$

In this highly simplified model, all inhomogenities in the chemical composition of the disk are neglected. The disk is assumed to consist entirely of individual gas particles with a mean molecular mass m_{mol}. The temperature is vertically isothermal and under the assumption of a constant aspect ratio (which is defined below) is proportional to $1/r$. If the gas were perfectly Keplerian, the trajectory of such a gas particle in the gravitational potential of a star with mass M_* would be described by Kepler's laws. Assuming a circular orbit, the angular frequency could then be expressed as

$$\Omega_K = \sqrt{\frac{GM_*}{r^3}} \tag{1.2}$$

In reality, the gas in a disk does not orbit its parent star in a perfectly Keplerian way, with lower rotation velocities than one would expect from Equation 1.2. This is due to the pressure gradient in the disk, which effectively leads to a decreased gravity felt by the gas. If, additionally, a planet is present in the disk and its interactions with the gas are taken into account, the trajectories of individual bodies (planet or gas particles) in this system become impossible to determine analytically, therefore making the utilization of numerical simulations very attractive.

Since they mostly probe the outer domains of proto-planetary disks, millimeter observations as of yet do not give much information about the gas density profile in the inner regions of the disk (Dullemond and Monnier, 2010). A first approach to modeling the gas surface density's dependency on r is to assume a simple power law:

$$\Sigma(r) = \Sigma_0 \cdot \left(\frac{r}{r_0}\right)^{-\gamma} \tag{1.3}$$

In our case, r_0 labels the distance of the planet from the star and $\Sigma_0 := \Sigma(r_0)$ is the surface gas density at the position of the planet. The slope of $\Sigma(r)$ is characterized by the parameter γ, which is assumed to be equal to 1 in thesis.

Even though the disk will be treated as a 2D object in this thesis, it is important to talk about the geometry of real disks observed in the night sky. Contrary to what one might expect without any prerequisite knowledge, observations show that the spatial extension in z-direction of proto-planetary disks grows larger with increasing distance from the star. An approximation of this can be made by expressing the surface scale height H as a polynomial function of the distance from the center r. With $H_0 := H(r_0)$, this can be written as

$$H(r) = H_0 \cdot \left(\frac{r}{r_0}\right)^{\beta} \tag{1.4}$$

Here, β labels the so-called *flaring index*. A disk with $\beta > 0$ is called a *flared disk*. Throughout most of this thesis, we will assume a non-flared disk with $\Sigma(r) = \Sigma_0$, i.e. $\beta = 0$. A sketch of a non-flared as well as a flared disk can be seen in Figure 1.2.

Equation 1.4 suggests the definition of another useful parameter, namely the *aspect ratio*

$$h_r(r) := H(r)/r \tag{1.5}$$

A commonly used value to set up the disk's ratio of height to width is $h_r(r_0) = 0.05$ (see e.g. Kley, W., 1999), which will be used in most of the simulations discussed in this thesis.

To model the disk's viscosity, the α-description is used:

$$\nu = \alpha_{visc} \cdot \frac{c_s^2}{\Omega_K} \tag{1.6}$$

It is assumed that the parameter α_{visc} is constant throughout the disk and does not change with time. Observations of real proto-planetary disk show typical values to be roughly around 10^{-4} (e.g. Dullemond et al., 2018), whereas for numerical simulations the alpha parameter is often assumed to be a few magnitudes smaller, and is commonly set to $\alpha_{visc} = 10^{-2}$ (e.g. Bailli, Charnoz, and Pantin, 2016). Here we remain agnostic about the different alpha values and use $\alpha_{visc} = 10^{-4} - 10^{-2}$. The viscous evolution of the gas surface density over time is taken from Lynden-Bell and Pringle (1974), where it is expressed as

$$\frac{\partial \Sigma}{\partial t}(r,t) = \frac{3}{r} \cdot \frac{\partial}{\partial r}\left(\sqrt{r} \cdot \frac{\partial}{\partial r}\nu \cdot \Sigma(r,t) \cdot \sqrt{r}\right) \tag{1.7}$$

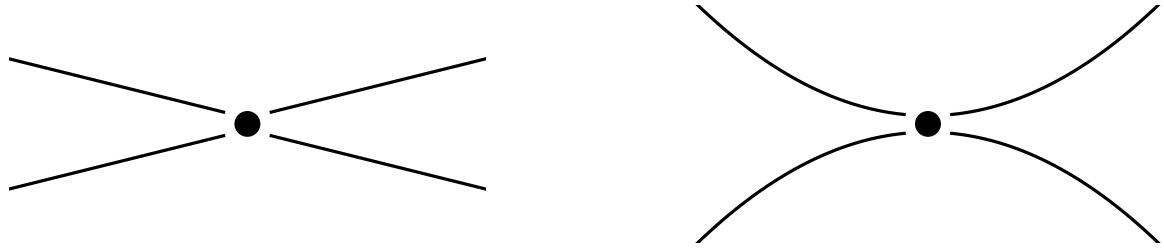

(a) non-flared disk (b) flared disk

Figure 1.2: Qualitative sketches of the difference between flared and non-flared disks

1.3 Planets in the Disk

1.3.1 Planet Formation

Most standard planet formation theories assume the initial buildup of a central rocky core [21]. From this point on, the proto-planet may either develop into a terrestrial planet or into a giant planet consisting of a rocky core and a large gaseous hull. In our own Solar System, the four terrestrial planets are those situated closest to the Sun, while the four gas and ice giants sit in the outer regions of the Solar System.

This is probably no coincidence. Most of the matter in the universe, and therefore most likely also most matter in newly formed disks, consists of light elements like hydrogen and helium. Because of the radiation pressure of the solar wind, these light elements accumulate in the outer regions of the disk. Therefore, an accreting planetoid in the outskirts of the disk has much more material available for accretion in its vicinity than one positioned close to the center.

In the early stages of planet formation, gravity does not play a dominant role. Gas and dust grains collide and stick together mainly via microphysical processes like van der Waals or Coulomb forces (Ward, William R., 1996). These processes are not still entirely understood today. It is unclear how the early planet cores manage to grow without fragmenting into smaller pieces again at collisions with other, similarly-sized planetesimals (Morbidelli and Raymond, 2016).

The early development of planetesimals will not be studied in this thesis. It is assumed that the initial buildup of a planet core has already taken place. From this point on, planets grow either by direct collisions with other bodies or via gravitational capture of gas (Morbidelli and Raymond, 2016). This leads to the eventual formation of circumplanetary accretion disks similar to the proto-planetary disk itself, but on much smaller scales.

The accreted material comes mostly from inside the planet's Hill sphere (also called the Roche sphere). This is the region in space where the gravitational influence of the planet's is larger than that of its central star (Hamilton, D. P. & Burns, J. A., 1992). If a body with mass m orbits a larger mass M with a semi-major axis a and eccentricity e, the radius of the Hill sphere can be approximated by

$$r_H \approx a(1-e)\sqrt[3]{\frac{m}{3M}} \tag{1.8}$$

To simulate a proto-planetary disk, this thesis makes use of the *FARGO2D1D* algorithm, which will be discussed in detail in section 2.1. The code handles accretion by including both a Kley and a Machida accretion subroutine, which are also given a detailed description in that section. Since the accretion process is a highly complex process including a very large number of individual particles, this can not be simulated in detail and simplifications have to be made. The Kley and Machida accretion constitute one way of doing this, but many different models of accretion have been suggested, e.g. by Matsumura, Brasser, and Ida (2017), Morbidelli (2018) or Schulik et al. (2019).

For most simulations, the planet will be kept on a fixed orbit so that there is no migration.

1.3.2 Gap Formation

Recent observations of proto-planetary disks often show dark, circular regions around the star, as we already saw in the *ALMA* images in Figure 1.1. It is assumed that these are created by proto-planets that form in orbit around the star. When sufficiently grown, a proto-planet exerts tidal torques on the disk and thereby induces trailing spiral shocks (Kley, W., 1999). Via these, angualar momentum is transfered between the disk and the planet, which has the effect of material being pushed away from the proto-planet. To be more precise, the planet loses some of its angular momentum to the outer part of the disk, while it receives some from the inner part.

This process eventually leads to the the opening of a gap in the disk. The criteria for gap opening depend on the the viscosity, pressure and planetary mass. They are discussed in detail in Lin & Papaloizou (1986, 1993) as well as Crida, Morbidelli, and Masset (2006). The width of the gap, i.e. extent in radial direction, also depends on the mass of the planet, as well as the viscosity and gas pressure in the disk (Lin and Papaloizou, 1993).

After the formation of the gap, there is still accretion from regions outside or inside the planet's orbital radius, since the internal evolution of the disk tends to spread the gas back into the void regions by diffusion (Kley, W., 1999). Thus, the accretion rate after gap opening has occurred is further influenced by the thickness of the disk as well as the viscosity of the gas.

1.3.3 Migration

The interaction of a growing proto-planet with the gas in the disk can lead to a change in the orbital parameters of the proto-planet, most importantly a change in the planet's semimajor axis, i.e. migration of the planet (Dürmann and Kley, 2015). Depending on the mass of the planet, different categories can be distinguished to describe the migration.

For low-mass planets not massive enough to open up a gap in the disk (less than about 50 Earth masses), the occuring change in the orbital elements is commonly labeled as *type I migration*. We will not focus on this type of migration, since all planets in this thesis have masses on similar orders of magnitude as Jupiter.

For massive planets that are able to form a gap, *type II migration* occurs. During the migration period, the gap will move through the disk with the planet. It is often assumed that in an equilibrium situation, the gap moves at exactly the same speed as the planet, and that the planet is locked in the middle of the gap to maintain torque equilibrium (Dürmann and Kley, 2015 and Lin and Papaloizou, 1986) and thus migrates with the viscous evolution of the disk. However recent simulations done by e.g. Dürmann and Kley (2015) or Robert et al. (2018) have shown that this is not true. In particular the studies by Kanagawa, Tanaka, and Szuszkiewicz (2018) indicate that the migration rate scales with the depth of the gap.

Chapter 2

Methods

2.1 The *FARGO2D1D* Algorithm

The *FARGO* algorithm was originally introduced by Masset, F. (1999). The algorithm's name is an acronym for *Fast Advection in Rotating Gaseous Objects*. It is written in *C* and utilizes a 5th order *Runge-Kutta* subroutine to determine the trajectory of a planet in the disk, as well as a fluid dynamics subroutine for the gas. It is possible to configure whether the planet should interact only with its parent star or also with the gas in the disk, allowing for simulations of planet migration. The gas feels the gravitational potential of the star and the planet. Accretion of gas onto the planet is handled in a simplified way, which will be discussed over the next few paragraphs.

To model a protoplanetary disk, it is represented in the code simply by a 2D grid. Each grid cell stands for a specific location in the disk. The row and column of such a cell correspond to its radial and azimuthal position.

In this thesis, an extension of the standard version of *FARGO* is utilized, titled *FARGO2D1D*. Here, the 2D grid is surrounded by an additional, one-dimensional grid made up of elementary rings. The planet is placed within the 2D section of the grid. Far from the center, the gravitational influence of the planet on the structure of the disk is diminishingly small [14]. Because of this, the disk can be assumed to be axisymmetric for both very small and very large values of r.

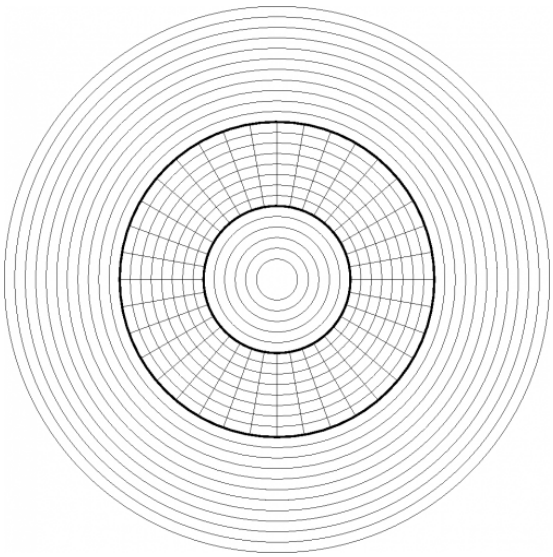

Figure 2.1: Sketch of the grid that is being used by the *FARGO2D1D* algorithm [13]. It consists of both a one-dimensional section and a two-dimensional section. In the latter, the planet is placed.

The algorithm in principle allows to have multiple planets in a single disk, all interacting with each other as well as with the disk. In this thesis though, only a single planet is inside the disk at any given time. At $t = 0$, the disk's surface density profile is initialized according to Equation 1.3. In the following time steps the planet is introduced to the disk.

To prevent disruptive shocks or numerical artifacts from arising at the introduction of the planet to the disk, its mass is first set to 0 and then slowly increased over the next few time steps. This time span will be referenced as *tapering period* hereafter. After the tapering period, the planet's mass then is equal to the inital mass value m_0 specified in the configuration files. The planet's intial velocity vector is set up in such a way as to position it on an orbit around the star, the eccentricity of which can be manually specified.

To give the disk some time to settle into an equilibrium state, accretion does not start directly after the tapering has finished. Instead, the accretion subroutine is deactivated for a time span that shall be called *accretion wait*.

After the period of accretion wait is over, the planet can finally start gathering mass. This is realized in the code by an accretion subroutine, which consists of two parts. Both the *Kley* and *Machida* accretion rates, which will be explained in detail below, are calculated at each time step. Afterwards, the minimum value of these two is used to determine the amount of mass removed from the disk and added to the planet.

2.1.1 Accretion Mechanisms

To simulate gas accretion onto a planet, the following approach is used: After each time step Δt, a mass amount Δm is removed from the grid cells inside the Hill sphere and added to the planet.

$$m_{disk}(t + \Delta t) = m_{disk}(t) - \Delta m \tag{2.1}$$

$$m_{planet}(t + \Delta t) = m_{planet}(t) + \Delta m \tag{2.2}$$

The precise value of Δm is determined by making use of two different models, namely a slightly modified version of both the accretion recipe given by Kley, W. (1999) as well as the one given by M. Machida et al. (2010). Both accretion rates are calculated in each timestep, then the minimum of these two values is used.

$$\Delta m = \min\Big(\Delta m_{Kley};\ \Delta m_{Machida}\Big) \tag{2.3}$$

Machida Accretion

In the code, a variant of the accretion formula used by M. Machida et al. (2010) is utilized, which was derived from 3D isothermal simulations. In each time step, the amount of mass to be removed from the Hill sphere is given by

$$\Delta m_{Machida} = \Sigma(r,t) \cdot H^2 \cdot \Omega \cdot \min\Big(0.14;\ 0.83 \cdot (r_H/H)^{9/2}\Big) \cdot \Delta t \tag{2.4}$$

Kley Accretion

Additionally to the Machida accretion, we will use a modified version of the accretion recipe suggested by Kley, W. (1999). The precise value of Δm is determined via

$$\Delta m = f_{red} \cdot S_{acc} \cdot \Sigma(r,t) \cdot f_{acc} \cdot \Delta t \tag{2.5}$$

Here, S_{acc} is the size of the disk surface inside the planet's Hill sphere, $\Sigma(r,t)$ is the gas surface density at a distance r from the planet's center at time t. With the parameter f_{acc}, the overall accretion rate can be tweaked and f_{red} determines from where precisely in the Hill sphere mass is removed. The latter is defined as

$$f_{red} = \begin{cases} \frac{2}{3} & \text{if } r/r_H < 0.45 \\ \frac{2}{3} \cdot \cos^4\left(r/r_H - 0.45\right) & \text{if } 0.45 \leq r/r_H \leq 0.95 \\ 0 & \text{if } r/r_H > 0.9 \end{cases} \tag{2.6}$$

A visualization of the r-dependence of f_{red} can be seen in Figure 2.2.

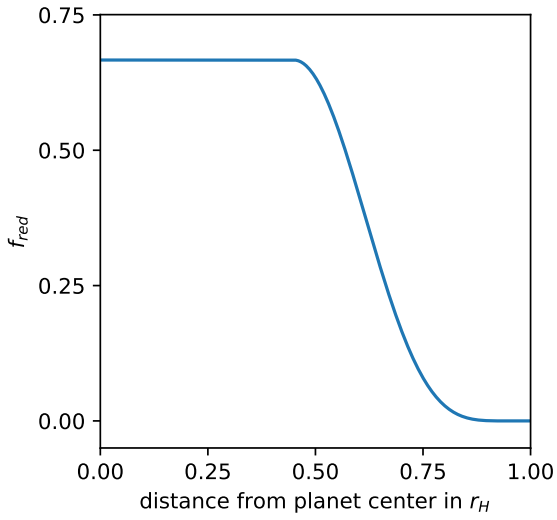

(a) r-dependence of f_{red}

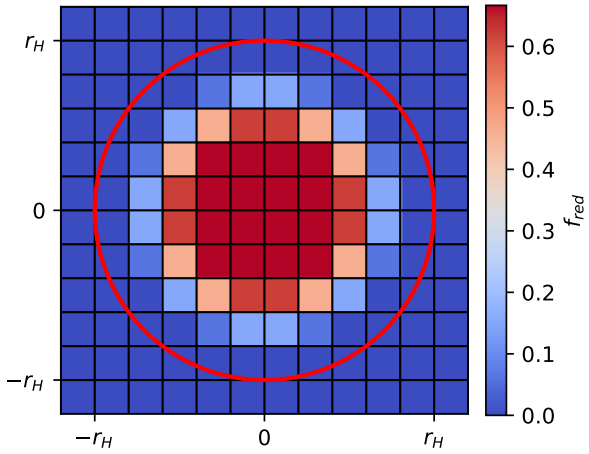

(b) Visualization of the value of f_{red} in the grid, the red circle marks the boundaries of the Hill sphere.

Figure 2.2: Smoothing function f_{red} that determines where and how much mass is to be taken by the Kley accretion subroutine out of the planetary Hill sphere at each time step.

2.1.2 Code Units

In astronomy, one often has to deal with large numbers, e.g. the solar mass is $M_\odot \approx 1.989 \times 10^{30}\,\mathrm{kg}$. To make things easier, we will utilize a different system of measurement units in this theis, which will be referenced as *code units* hereafter.

In this system, the basic measuring unit of mass is that of the sun, (i.e. $M_\odot = 1$). The mass accretion rate $\dot{m}$ of a planet is measured in solar masses per orbit. Spatial lengths are measured in multiples of the average distance between Jupiter and the sun, which in SI units amounts to about 5.2 au. All of the simulated planets in this thesis will initially be positioned at this distance, i.e. $r = 1$.

The mass of the central star is assumed to be much larger than that of the planet. Also, the Newtonian gravitational constant G is set to unity as well. Under these assumptions, the Keplerian angular velocity is simply $\Omega_K = 1$ and the period of one orbit of a planet (at $r = 1$) around the star is $T = 2\pi$.

2.1.3 Default Parameters

If not otherwise specified, the following configuration values will be used by default:

Table 2.1: Default simulation parameters

parameter	value
aspect ratio h_r	0.05
flaring index β	0
surface density $\Sigma(r = 0)$	$3 \cdot 10^{-4}$
sigma slope γ	1
viscosity parameter α_{visc}	10^{-2}
mass tapering period	50 orbits
radial resolution N_{rad}	202
azimuthal resolution N_{sec}	456
lower boudary for 2D grid $R_{min,2D}$	0.2
upper boundary for 2D grid $R_{max,2D}$	5
lower boundary for 1D grid $R_{min,1D}$	0.02
upper boundary for 1D grid $R_{max,1D}$	50

With these parameters, we can calculate the total mass of the simulated part of the disk:

$$m_{disk} = 2\pi \int_{0.02}^{50} \Sigma(r = 0) \cdot r^{-\gamma} \cdot dr \approx 0.015\ M_\odot \tag{2.7}$$

2.2 First Runs

To get a general idea for the behavior of simulated disks over time, see Figure 2.3. Here, a top-down view on the disk is shown, which is visualized in polar coordinates for various times. The color coding corresponds to the value of the the gas surface density on a logarithmic scale. The influence of the planet's momentum exchange with the gas is clearly visible in the forming spiral arms and the gap, which grows deeper and wider with time.

In Figure 2.4, an analogous plot can be seen, this time for a planet on an eccentric orbit ($e = 0.3$). Here, the disk evolvution is more chaotic. The gap formed by the planet is also much wider, which will be discussed in more detail later in this thesis, when the effect of the orbital eccentricity on the structure of the gap and therefore on the accretion rate will be investigated.

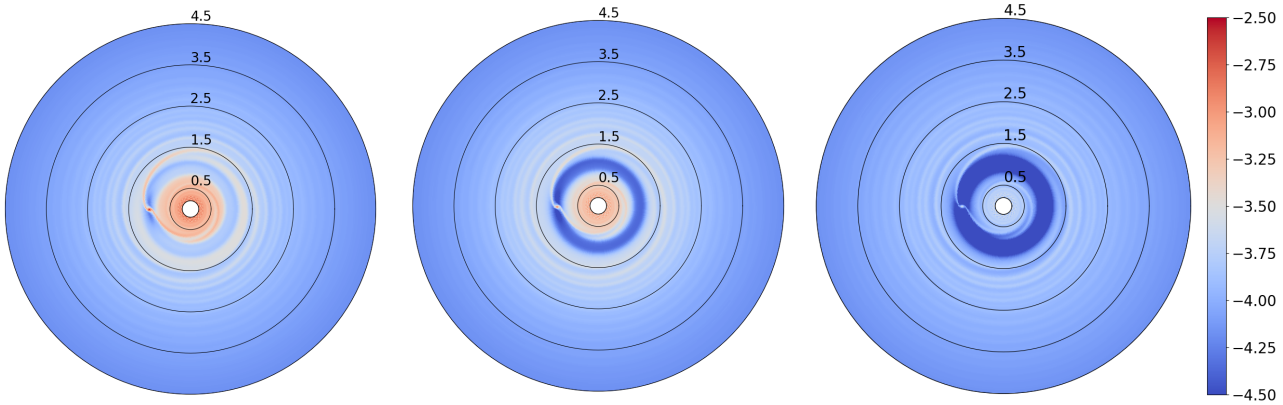

(a) after 50 orbits (b) after 500 orbits (c) after 2500 orbits

Figure 2.3: Evolution of gas surface density over time for a non-migrating, non-accreting planet of initial mass $m_0 = 1\ M_{jupiter}$ on a circular orbit. The disk parameters are $\alpha_{visc} = 10^{-2}$, $h_r = 0.05$. The exchange of angular momentum between gas and planet can be recognized by the formation of a gap in the disk.

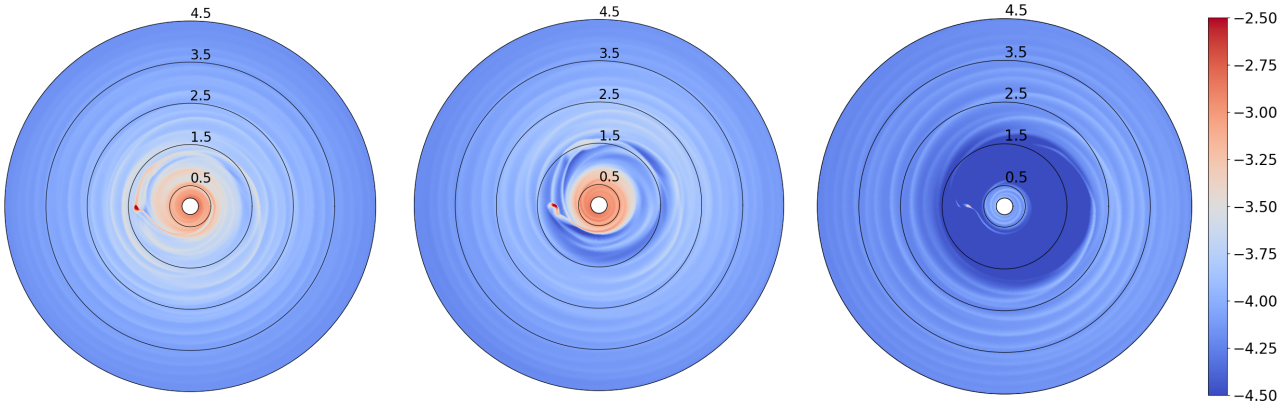

(a) after 50 orbits (b) after 500 orbits (c) after 2500 orbits

Figure 2.4: Evolution of gas surface density over time for a non-migrating, non-accreting planet of initial mass $m_0 = 1\ M_{jupiter}$ on an elliptic orbit of eccentricity $e_{planet} = 0.3$. The disk parameters are $\alpha_{visc} = 10^{-2}$, $h_r = 0.05$. The exchange of angular momentum between gas and planet can again be recognized by the formation of a gap in the disk, which is more wide than in the case of a circular orbit. The gap itself also possesses an eccentricity $e_{gap} \neq 0$, which increases both with e_{planet} and m_0.

2.3 Choosing the Resolution of the 2D Grid

The *FARGO2D1D* algorithm defines the resolution of the 2D grid via the two variables N_{rad} and N_{sec}, which designate the number of grid cells in radial and azimuthal direction, respectively. To find the optimal simulation resolution, a compromise has to be found between the integration time and the accuracy of the simulation results. Before this is done though, the optimal ratio between the radial resolution N_{rad} and the azimuthal resolution N_{sec} has to be found:

The grid is treated by the algorithm simply as a 2D rectangular matrix. In reality though, the system is of course not rectangular, but circular. The projection of the rectangular grid into polar coordinates leads to a distortion of the square grid cells. The grid cells that are very close to the center as well as those very far away from the center are subject to strong distortions.

To make sure that the accretion subroutine functions accurately, the resolution should be chosen in such a way that the grid cells' shape is as close to a square as possible at the radial position of the planet (i.e. at $r = 1$). For that, let's take a look at Figure 2.5, which visualizes a radial grid section at a distance r from the center.

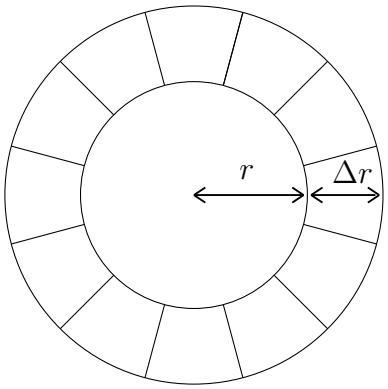

Figure 2.5: Sketch of a radial division in the simulation grid

To be as close to a square as possible, each azimuthal ring division should ideally have an area of

$$A_{cell} \approx \Delta r^2 \tag{2.8}$$

The total area of the ring is given by

$$A_{ring} = \pi(r + \Delta r)^2 - \pi r^2 = \pi(2r\Delta r + \Delta r^2) \tag{2.9}$$

Utilizing the relation $N_{sec} = A_{ring}/A_{cell}$ and then plugging in $r = 1$, this yields

$$N_{sec} = \pi\left(\frac{2}{\Delta r} + 1\right) \tag{2.10}$$

The width of the ring Δr can be determined from the radial resolution and boundaries via

$$\Delta r = \frac{r_{max} - r_{min}}{N_{rad}} \tag{2.11}$$

It should now be clear how to easily calculate the optimal value of N_{sec} for any value of N_{rad}. Still, a few test simulations need to be run before one can decide on the resolution which optimizes the trade-off between integration time and accuracy.

To get a sense of the resolution's influence on the accuracy of the results, simulations are to be run for multiple different resolutions, namely 2.5, 5 and 10 cells per Hill radius. For each number $N_{c/rH}$ of cells per Hill radius, N_{rad} can be calculated via

$$N_{rad} = N_{c/rH} \cdot \frac{r_{max} - r_{min}}{r_H} \tag{2.12}$$

From this, N_{sec} can be determined with Equation 2.10 and Equation 2.11. This yields:

Table 2.2: Resolutions values for various numbers of grid cells per Hill radius for $m_{planet} = 1\ M_{jupiter}$

cells per r_H	N_{rad}	N_{sec}
2.5	101	230
5	202	456
10	404	909

Figure 2.6 visualizes how the planet's Hill sphere is implemented in the 2D array. For the simulations, a planet on a circular orbit with an intitial mass of 1 $M_{jupiter}$ is used, which builds up during a taper period of 10 orbits. After these 10 orbits, the planet starts accreting mass from its surroundings.

The radial gas density profile after a total of 500 orbits can be seen in Figure 2.7 on the next page. There is some discrepancy for small radii, but the overall structure of the gas density profile seems to be pretty much the same. To look at the behavior near zero, Figure 2.8 shows a zoomed in view of the disk. As can be seen here, a resolution of 2.5 cells per Hill radius leads to artifacts near the center, which disappear for higher resolution values.

Since the Hill radius increases with the planet's mass (see Equation 1.8), the number of grid cells inside the Hill radius will grow as time progresses and the planet accretes more material. Thus, these values of N_{c/r_H} only form lower limits and actually get better over time. It has already been shown by Lega et al. (2015) that at least 5 cells per Hill radius are necessary to accurately model planet migration. Because this resolution still offers the advantage of faster computation times by a factor of 8 relative to having 10 cells per Hill radius, all subsequent simulations are run with

$$N_{rad} = 202 \text{ and } N_{sec} = 456$$

if not otherwise specified.

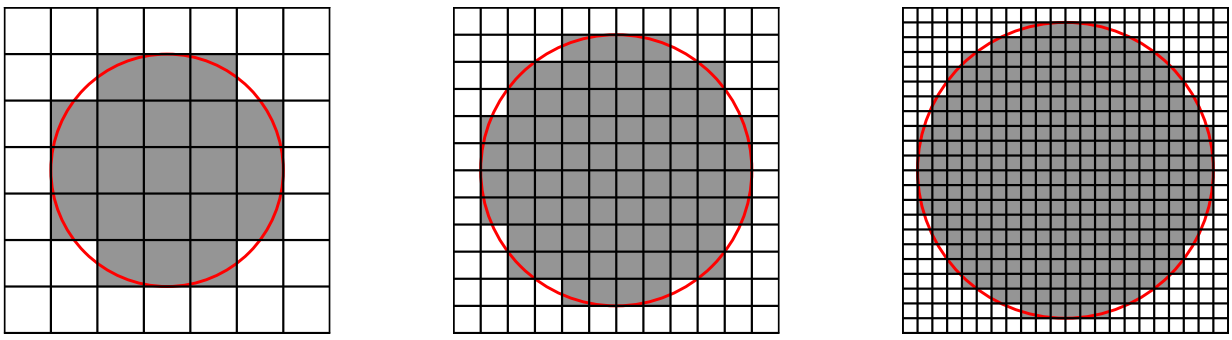

(a) 2.5 cells per r_H (b) 5 cells per r_H (c) 10 cells per r_H

Figure 2.6: Visualization of Hill spheres in the grid for various resolutions

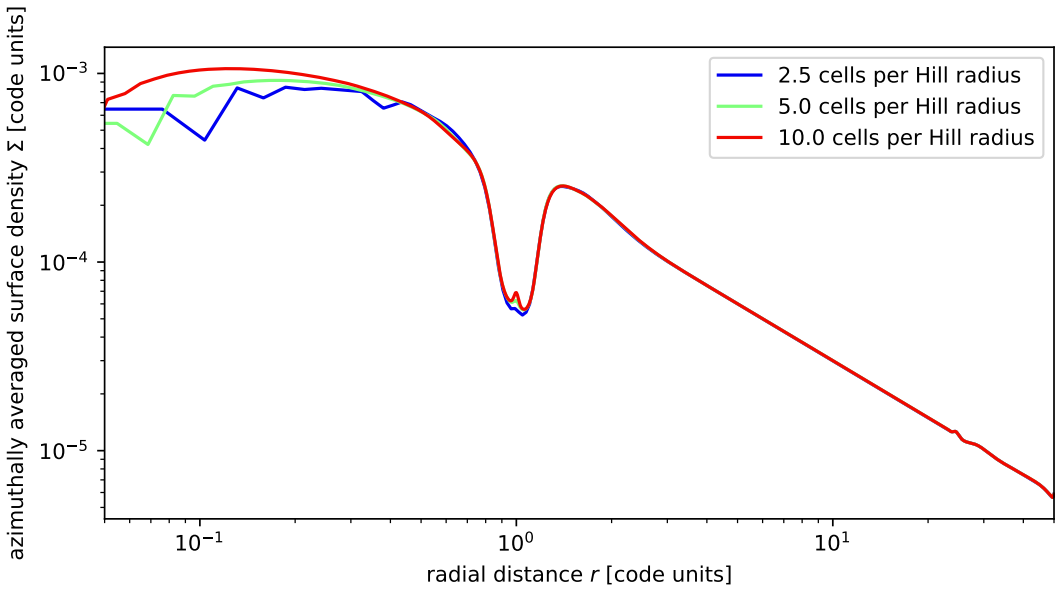

Figure 2.7: Azimuthally averaged surface densities at $t = 500$ orbits for three different grid resolutions. A single planet is positioned at $r = 1$. Its mass is initialized to $m_0 = 1\ M_{jupiter}$ during a tapering period of 5 orbits. Accretion starts at $t = 10$ orbits. Thus, the planet undergoes accretion for a total of 490 orbits. The planet is put on a circular orbit, migration is turned off and the disk is characterized by the parameters $\alpha_{visc} = 10^{-2}$, $h_r = 0.05$. The general structure of the gas density follows approximately the same course for all resolution values, with discrepancies being the largest for small values of r.

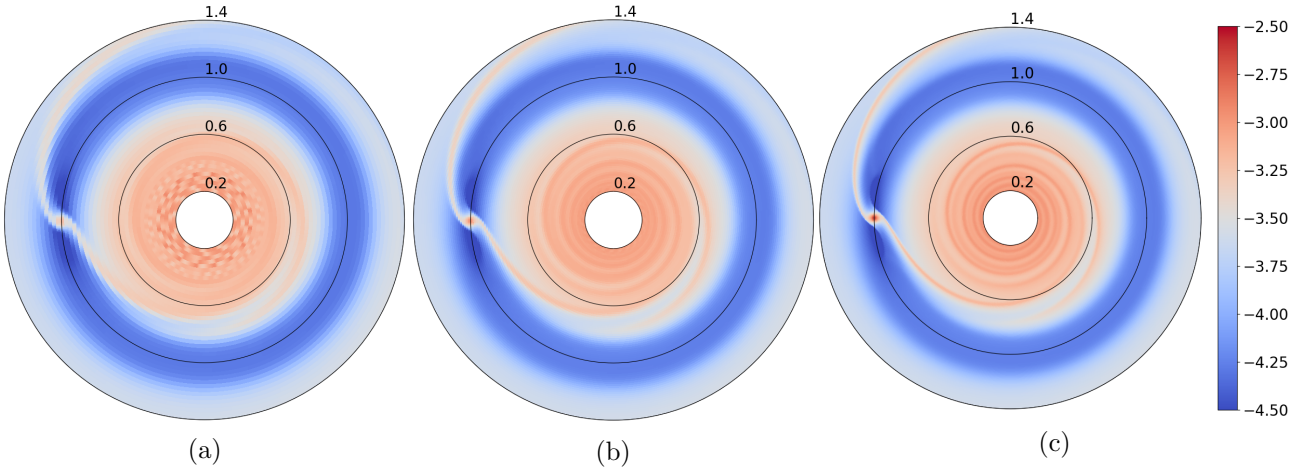

Figure 2.8: Gas surface density in the inner regions of the 2D grid for different resolutions at $t = 500$ orbits. The planet's mass is initialized to $m_0 = 1\ M_{jupiter}$ during a tapering period of 5 orbits. Accretion starts at $t = 10$ orbits. Thus, the planet undergoes accretion for a total of 490 orbits. The planet is put on a circular orbit and migration is turned off. The disk is characterized by the parameters $\alpha_{visc} = 10^{-2}$, $h_r = 0.05$. The black rings indicate the distance from the center, the color bar displays the order of magnitude (decadic logarithm) of the gas density in code units. For the lowest resolution, artifacts can be observed near the center of the disk, which disappear at higher resulution. Each doubling of the number of cells per Hill radius leads to a factor 8 increase in the needed computation time. Therefore, in this thesis we focus on simulations that initially have 5 grid cells per Hill radius.

2.4 Parameter Studies of the Disk

In this section, we investigate how the gas accretion rate onto the planet as well as the structure of the gap are influenced by the disk's characteristics, namely its geometry and the viscosity of the gas within the disk.

2.4.1 Disk Geometry

In our model, the geometry of the disk is mainly characterized by the aspect ratio h_r as well as the flaring index β. Let us first take a look at the influence of the aspect ratio. Simulations were carried out for various values of h_r with an integration time of 2500 orbits. During the first 50 orbits, the planet mass is slowly increased to 1 $m_{jupiter}$. Accretion starts at $t = 500$ orbits. The results can be seen in Figure 2.9a, where the gas density profile in the vicinity of the planet plotted as a function of the distance r from the disk center, and Figure 2.9, where the relative mass increase of the planet is plotted against h_r.

Higher values of the aspect ratio lead to a less deep gap, as has already been stated by Crida, Morbidelli, and Masset (2006). This is to be expected, since in a thicker disk more material is available and therefore more gas diffuses into the forming gap, hindering the planet from depleting the region.

One would expect that the accretion rate of the planet increases with the amount of gas in its Hill sphere. This is exactly what we see in Figure 2.9b. Thicker disks lead to faster gas accretion onto a planet in the disk. Furthermore, it seems that the relationship between aspect ratio and accretion rate is a linear one, at least in this simplified model.

The influence of the flaring index β is of a similar kind. Higher values of β lead to a shallower gap and higher accretion rate. Interestingly, the curves describing the surface density profile cross each other when varying the aspect ratio, but do not when varying the flaring index. Instead, Figure 2.10 shows what seems to be an additive offset between the gas profiles for different flaring indices. Increasing both h_r and β leads to a shallower gap, yet the surface density in disk regions around the gap grows with β and falls when increasing h_r.

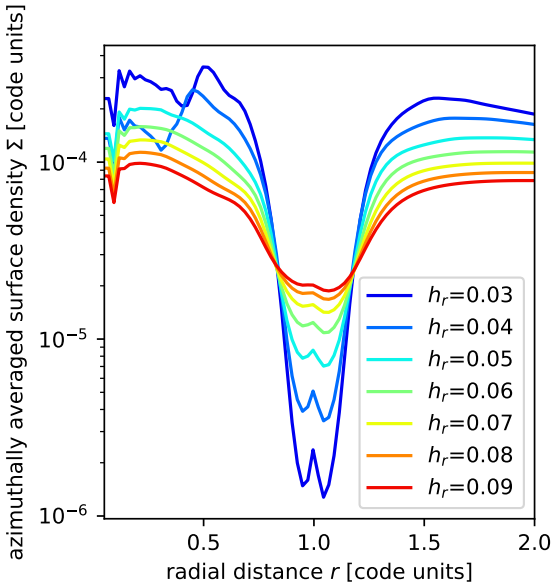

(a) surface density vs. aspect ratio

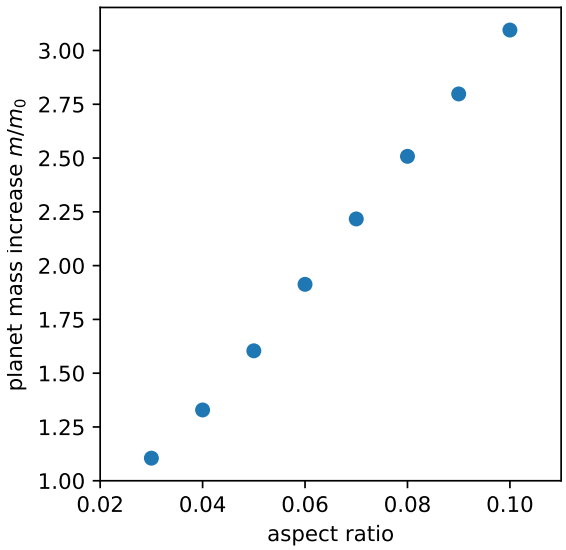

(b) increase of mass vs. aspect ratio

Figure 2.9: Influence of the disk's aspect ratio h_r on the gap profile and the increase of the planet's mass after an integration time of 2500 orbits. The first 50 of these orbits make up the tapering period (afterwards $m_0 = 1\ M_{jupiter}$) and the planet starts accreting after 500 orbits, the total duration of accretion is 2000 orbits. The planet is put on a circular orbit and migration is deactivated. The disk is characterized by the parameters $\alpha_{visc} = 10^{-2}$, $h_r = 0.05$. A thicker disk leads to more material diffusing into the forming gap, thus stifling its growth while accelerating accretion onto the planet.

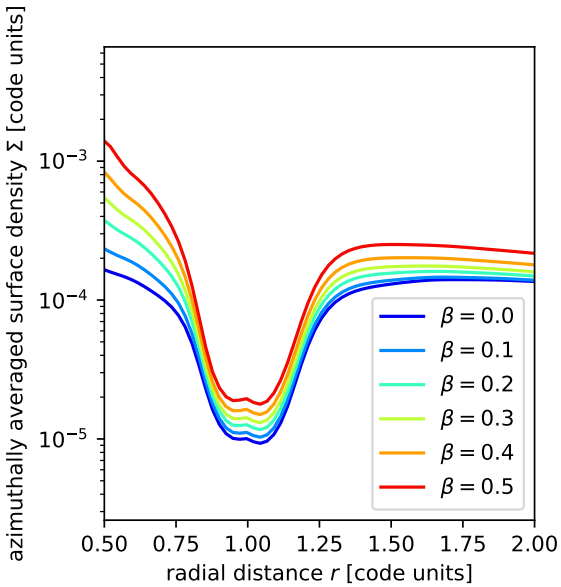

(a) surface density vs. flaring index

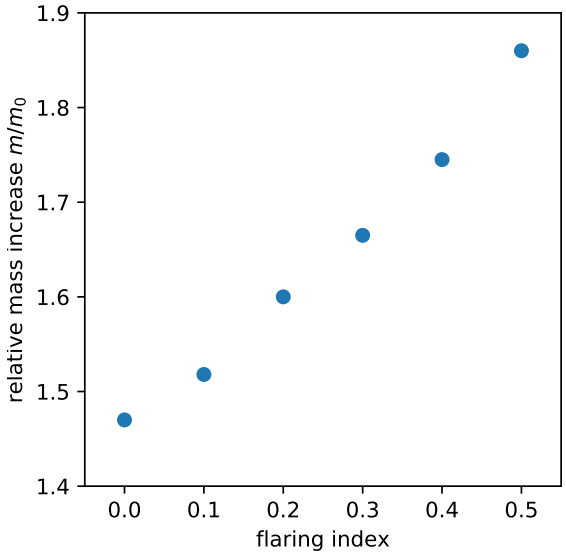

(b) increase of mass vs. flaring index

Figure 2.10: Gap profile and relative planet mass increase as a function of the disk's flaring index after an integration time of 2500 orbits. The first 50 of these orbits make up the tapering period (afterwards $m_0 = 1\ M_{jupiter}$) and the planet starts accreting after 500 orbits. Thus, the total accretion time has a duration of 2000 orbits. The planet is put on a circular orbit and migration is deactivated. The disk is characterized by the parameters $\alpha_{visc} = 10^{-2}$, $h_r = 0.05$. For higher values of β, the gap is less deep and the accretion rate increases.

2.4.2 Gas Viscosity Parameter

Next, we investigate the influence of the gas viscosity parameter α_{visc}. The simulations for this study were carried out using the same parameters as used in subsection 2.4.1, only this time the viscosity is not held constant. The aspect ratio is set to $h_r = 0.05$.

In Figure 2.11a, the gas surface density profile is plotted against the distance from the star. Large values of α_{visc} lead to a much less deep gap. While the planet's tidal influence due to gravity leads to a gas depletion in the regions close to its orbit, the material from further in- or outwards diffuses back in. If the gas is very viscous, this happens only slowly, and a gap can form. If, on the other hand, α_{visc} is large, the gap stays very shallow.

This is reflected in the relative mass increase that is plotted in Figure 2.11b. High values of α_{visc} lead to much more material being accreted by the planet, simply because there is that much more gas available in the its vicinity, analogous to what we saw for the parameter studies of the aspect ratio and flaring index.

A planet introduced to the disk pushes material away from its orbit, which then needs to diffuse away. For low values of α_{visc} this takes longer than for high values. This explains the fact that high alpha values lead to larger bump interior and exterior to the planets position.

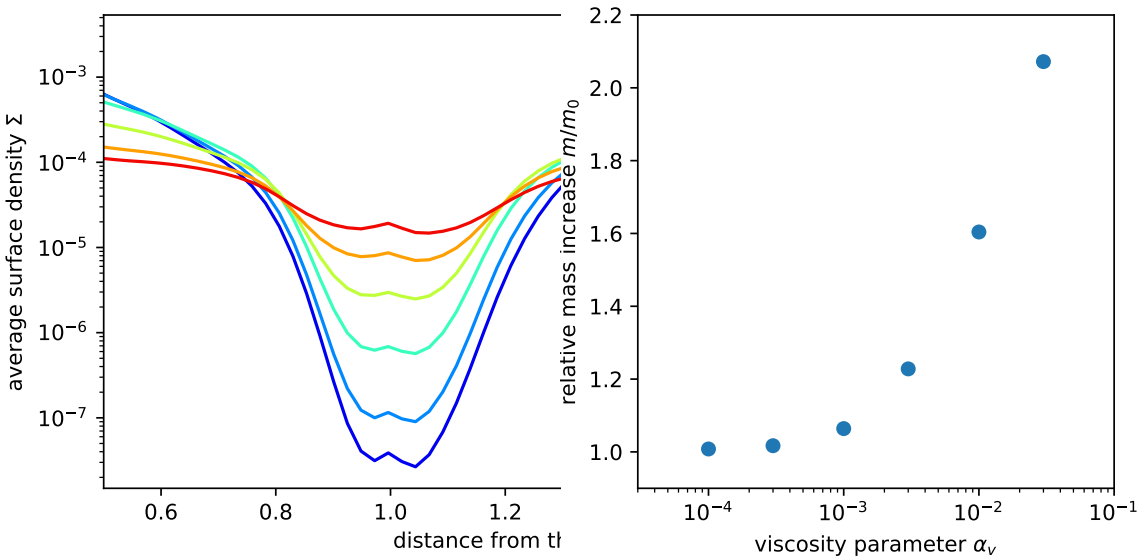

(a) surface density vs. viscosity (b) increase of mass vs. viscosity

Figure 2.11: Influence of the disk's viscosity parameter α_{visc} on the gap profile as well the relative planet mass increase after an integration time of 2500 orbits. The first 50 of these orbits make up the tapering period (afterwards $m_0 = 1\ M_{jupiter}$) and the planet starts accreting after 500 orbits. Therefore, the planet undergoes accretion for a total of 2000 orbits. It is initialized on a circular orbit and migration is deactivated. The disk is characterized by the parameters $\alpha_{visc} = 10^{-2}$, $h_r = 0.05$. The depth of the gap decreases with the viscosity parameter. Less viscous disks supply a faster inflow of gas into the low density regions created by the planet. Accretion accordingly grows with α_{visc}.

2.5 Parameter Studies of the Planet

It would be great to gain insight into how the features of the planet affect its accretion rate. To do this, we first vary the initial mass of the planet after tapering. Afterwards, we take a look at the influence of the eccentricity of the planet's orbit.

In the code, the accretion rate itself can be tweaked by scaling it up or down by a multiplicative factor. This is investigated as well, to find out how the gap structure and the relative increase in planet mass behave for high rates of gas accretion.

2.5.1 Initial Planet Mass

In Figure 2.12, the structure of the gap is displayed for various different values of the initial planet mass. Just as one would expect from earlier investigations by e.g. Kley and Dirksen (2006), planets with a larger mass carve out a deeper gap due to their greater exchange of angular momentum with the gas.

The opening of the gap of course directly influences the amount of gas in the Hill region of the planet and therefore its gas accretion rate, as can be seen in Figure 2.13, where the absolute and relative mass increase is displayed against the initial mass. Figure 2.14 shows the mass increase against time.

Relative to their own intital mass, the smaller planets experience the highest accretion rates.

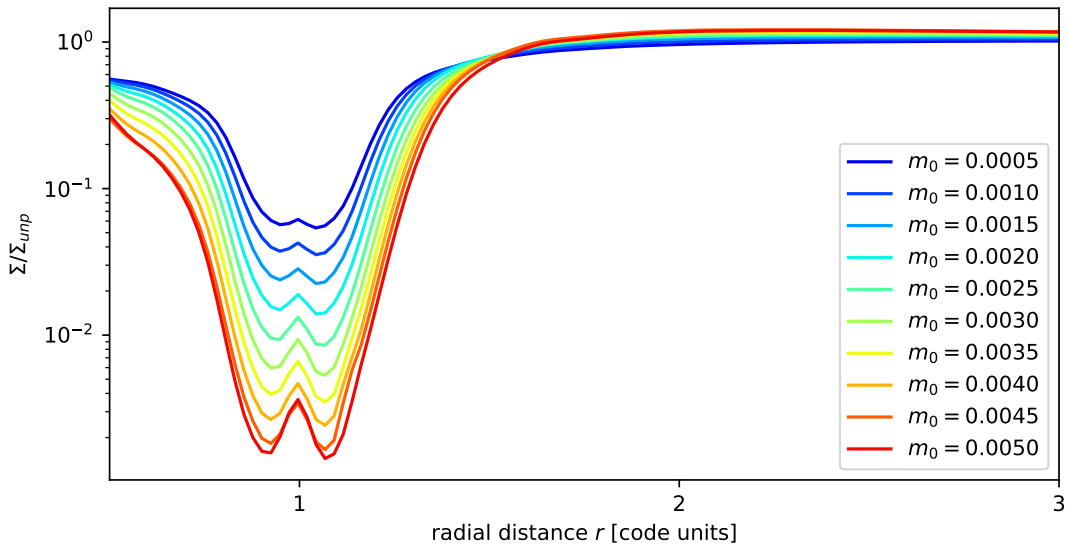

Figure 2.12: Surface density as a function of r for various initial planet masses after an integration time of 2500 orbits. The first 50 of these orbits make up the tapering period and the planet starts accreting after 500 orbits. Thus, the total accretion time has a duration of 2000 orbits. The planet is put on a circular orbit and migration is deactivated. The disk is characterized by the parameters $\alpha_{visc} = 10^{-2}$, $h_r = 0.05$. Due to their stronger interaction with the disk, high-mass planets carve out deeper and wider gaps than low-mass planets.

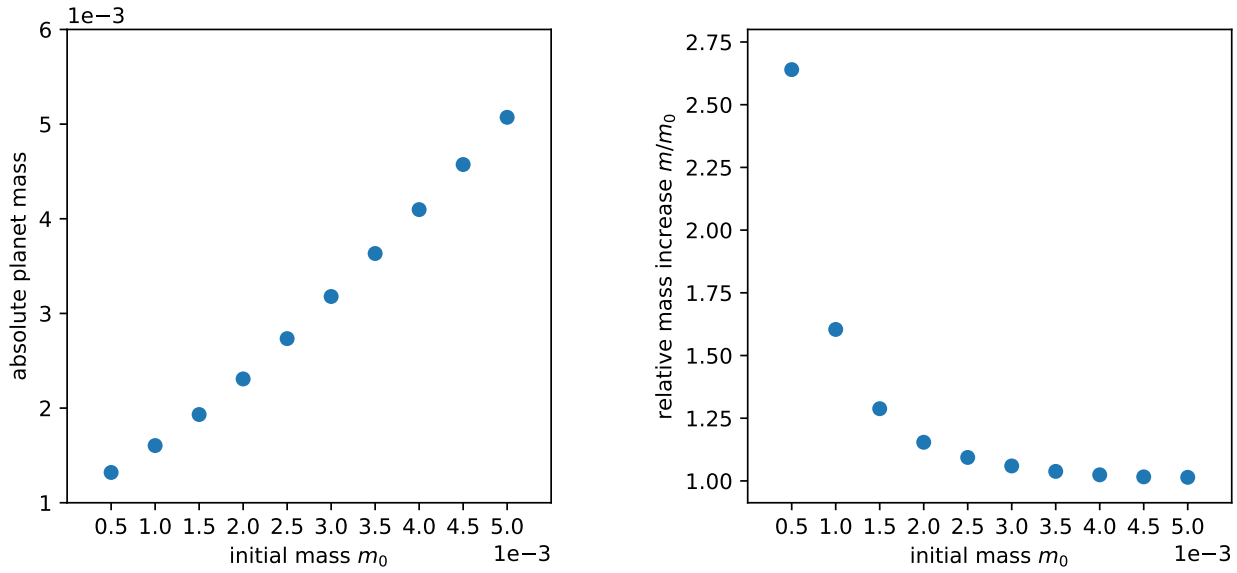

(a) absolute planet mass (b) relative mass increase m/m_0

Figure 2.13: Absolute and relative mass increase of a planet for various initial masses. The total integration time is 2500 orbits, of which the first 50 orbits make up the tapering period and the planet starts accreting after 500 orbits. Thus, the total duration of accretion is 2000 orbits. The planet is put on a circular orbit and migration is deactivated. The disk is characterized by the parameters $\alpha_{visc} = 10^{-2}$, $h_r = 0.05$. Low-mass planets experience faster accretion due them creating only small gaps.

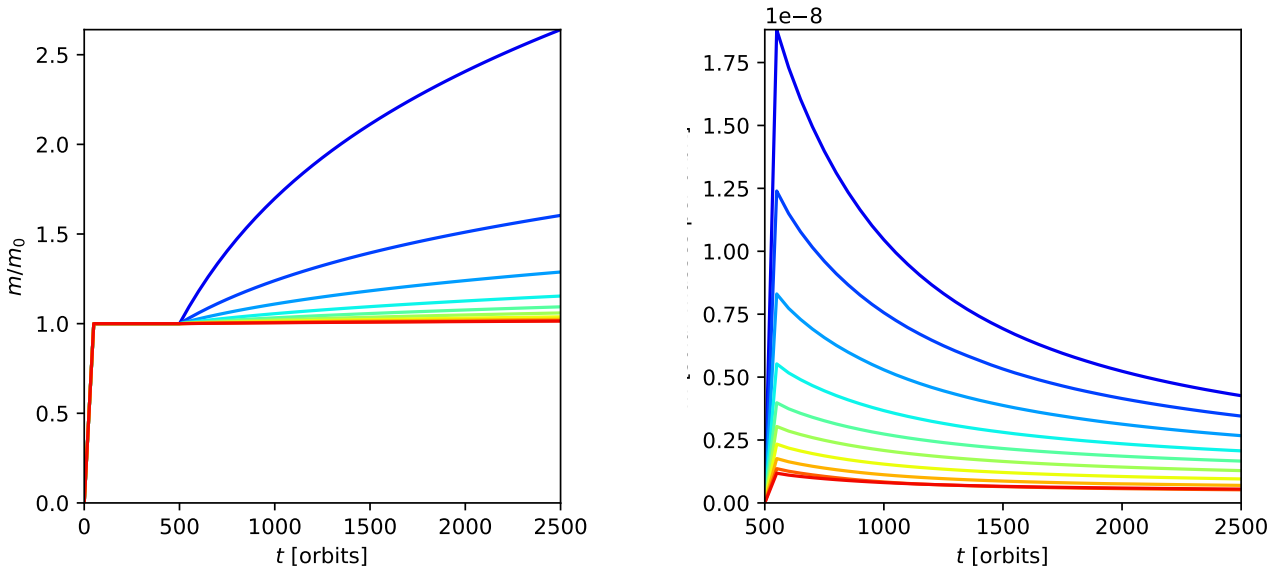

(a) mass increase vs. time and m_0 (b) accretion rate vs. time and m_0

Figure 2.14: Relative mass increase and accretion rate as a function of time for different initial planet masses. The integration time is 2500 orbits, of which the first 50 orbits make up the tapering period, the planet starts accreting after 500 orbits. Thus, the planet experiences accretion for a total 2000 orbits. The planet is put on a circular orbit and migration is deactivated. The disk is characterized by the parameters $\alpha_{visc} = 10^{-2}$, $h_r = 0.05$. Planets accrete the fastest when they're still small, because the gap they create is much more shallow compared to more massive planets.

Gas Surface Density Profile At Time Of Equal Accretion

It would be interesting to see what the profile of the gap looks like at times of equal accretion for various planet masses. If the accretion rate is the same, then it would make sense if the amount of gas in the Hill sphere of the planet were similar or the same as well.

Let us look at points in time at which the accretion rate on a planet is approximately equal to $6 \cdot 10^{-9}$ solar masses per orbit. Figure 2.15a attempts to visualize this. The times of interest are at the intersections between the black lines and the time axis. For each of these times, the surface density profile in the vicinity of the planet (divided by the unperturbed profile) is plotted in Figure 2.15b.

The gap profiles are quite similar, which becomes clearer when compared to what we already saw in Figure 2.12. To define a measure of how similar the gap profiles are for simulations with various planet masses, let us define the depth of the gap as $\Sigma(r = 1)$, which can be abbreviated to Σ_0. At times of approximately equal accretion, the ratio between the depth of the gap formed by a planet with $m = 0.5\ m_{jupiter}$ and the gap of a planet with $m = 1.5\ m_{jupiter}$ is

$$\frac{\Sigma_0(m = 0.5\ m_{jupiter})}{\Sigma_0(m = 1.5\ m_{jupiter})} \approx 1.5 \quad \text{(at times of equal acc. rate)}$$

while the gas densities shown in Figure 2.12 lead to a ratio of

$$\frac{\Sigma_0(m = 0.5\ m_{jupiter})}{\Sigma_0(m = 1.5\ m_{jupiter})} \approx 2.2 \quad \text{(after 2000 orbits of acc.)}$$

Thus, the gap profiles appear to indeed be more similar when comparing them at times of equal accretion than when comparing them after a fixed amount of time. That the gap profiles are not perfectly identical may partly be due to the fact that simulation output files were generated only every 50 orbits, so that the accretion rates are not exactly $6 \cdot 10^{-9}$ solar masses per orbit at these times.

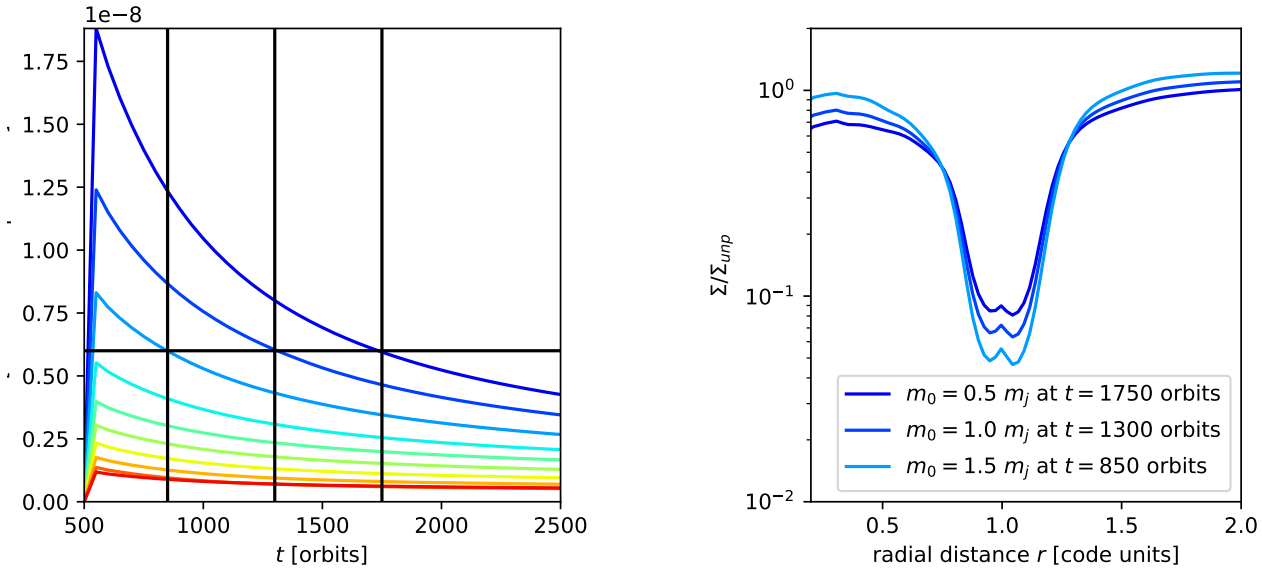

(a) mass increase vs. time and m_0

(b) gap profile

Figure 2.15: Comparison of gas density profiles at times of equal accretion. From the simulation results already shown in Figure 2.14a, we focus on the planets with the lowest mass, which meet the condition $\dot{m} \approx 6 \cdot 10^{-9}$ solar masses per orbit for different times. The gap profile is plotted for these times of equal accretion rates.

We can also calculate the mass inside the Hill sphere for each of the simulations. This yields

$$m_{Hill}(m = 0.5\ m_{jupiter}) = 5.5 \cdot 10^{-3}$$
$$m_{Hill}(m = 1.0\ m_{jupiter}) = 5.6 \cdot 10^{-3}$$
$$m_{Hill}(m = 1.5\ m_{jupiter}) = 5.9 \cdot 10^{-3}$$

As above, the relative differences between those values are probably explained by the fact that the accretion rate is not exactly the same, since outputs were only generated every 50 orbits. Even though the planet with $m = 1.5\ M_{jupiter}$ created the deepest gap, it also has the most matter in its Hill sphere. This can be attributed to the fact that the Hill sphere grows with the mass of the planet.

2.5.2 Numerical Accretion Rate

Let us take a look at the influence of the accretion rate of gas onto the planet, which can be tweaked in the code. Simulations are run for various factors between 0.5 and 3.0. The results can be seen in Figure 2.16.

As we increase the factor controlling the accretion rate, the gap grows deeper and the planet's mass increase grows larger, just as one would expect. It is interesting to see though that the relation between the relative mass increase and the accretion factor is not a linear one, but that the effect of the accretion factor on the mass increase seems to weaken for high values. This is due to the eventual depletion of the Hill region. The relative mass increase is limited for very high accretion factors by the gas inflow into the gap from regions further in- or outwards, which is set by the disk's viscosity.

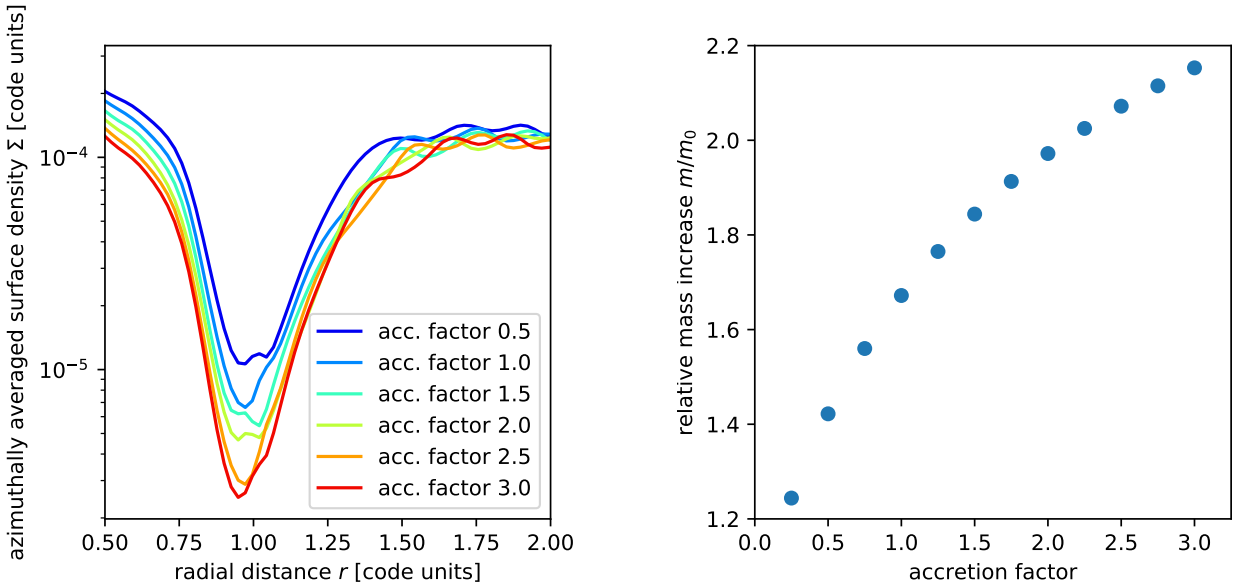

(a) radial gas density vs. accretion

(b) mass increase vs. accretion

Figure 2.16: Influence of the numerical accretion rate on the gap profile and the planet's mass increase after the end of a simulation with an integration time of 2500 orbits. The first 50 of these orbits make up the tapering period and the planet starts accreting after 500 orbits. Thus, the total accretion time possesses a duration of 2000 orbits. The planet is put on a circular orbit and migration is deactivated. The disk is characterized by the parameters $\alpha_{visc} = 10^{-2}$, $h_r = 0.05$. High accretion rates lead to a large increase in planet mass, obviously. The effect is less noticable for high values of the accretion factor though, because the regions near the planet become more and more depleted and accretion slows down.

2.5.3 Initial Planet Eccentricity

Up until now, we've almost exclusively investigated planets on circular orbits. Let us now turn our attention towards planets with orbital eccentricities $e \neq 0$. For the time being, the value of e is configured at the beginning of the simulation and then does not change over time, i.e. migration and eccentricity damping is turned off and the planet does not feel the gravitational potential of the disk, so that $e(t) = e_0 := e(t = 0)$. Simulations are run for various eccentricity values with an integration time of 2500 orbits. The first 50 orbits make up the tapering period and accretion is turned on at $t = 500$ orbits, after the gap has formed and the disk has reached a steady state.

Influence On The Profile Of The Gap

The surface density profile near the gap is plotted for $t = 500$ orbits (before accretion) in Figure 2.17a and for $t = 2500$ orbits (after accretion) in Figure 2.17b. Once again, the deepening of the gap over time via the planet's momentum exchange can be observed. Furthermore, it can be seen how the eccentricity influences the gap structure. Due to the periodic changes in the planet's distance from the star, the forming gap possesses a much wider profile for higher values of e_0. Consequently, its depth decreases for larger eccentricity values.

Figure 2.18 shows the azimuthally averaged surface density at the radial position of the planet (i.e. $\Sigma(r = 1)$) plotted against the eccentricity of the planet's orbit. The reasons for the existence of a minimum have been discussed by Thun, Kley, and Picogna (2017). This once again visualizes why planets on eccentric orbits undergo faster accretion, since there is more mass available in their immediate vicinity.

(a) before accretion ($t = 500$ orbits)

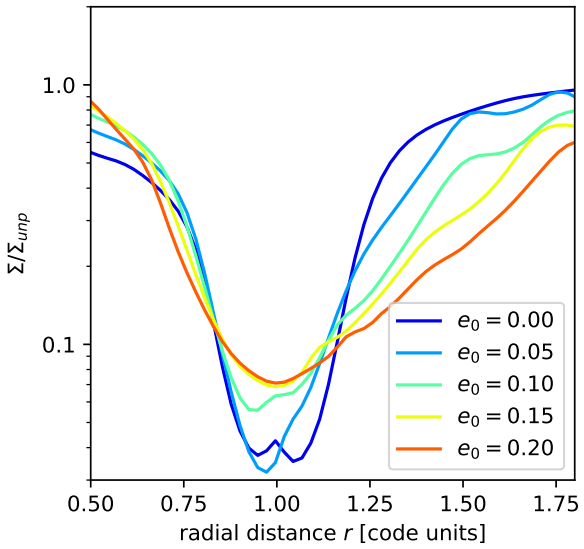

(b) after accretion ($t = 2500$ orbits)

Figure 2.17: Surface gas density as a function of r for various planet orbit eccentricites. The left and right plot show the gap profile for two different times, namely before and after an accretion period of 2000 orbits. In the beginning, accretion is turned of. The first 50 orbits make up a tapering period (after which $m_0 = 1\ M_{jupiter}$) and the planet starts accreting at $t = 500$ orbits. The total integration time therefore is 2500 orbits. Migration is deactivated and the disk is characterized by the parameters $\alpha_{visc} = 10^{-2}$, $h_r = 0.05$. The gap grows deeper with time, larger eccentricites lead to wider, yet more shallow gaps.

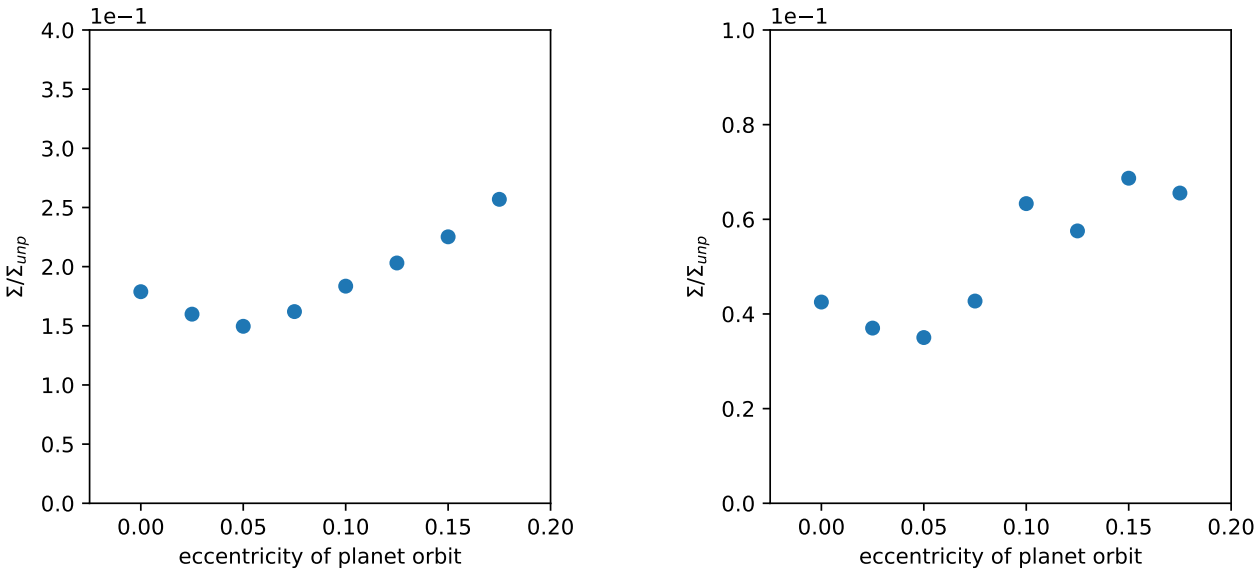

(a) before accretion $t = 500$ orbits

(b) after accretion ($t = 2500$ orbits)

Figure 2.18: Gap depth (i.e. $\Sigma(r = 1)$) vs. planet orbital eccentricity. $t = 2500$ orbits. The first 50 orbits make up the tapering period, after which $m_0 = 1\ M_{jupiter}$. The planet starts accreting after 500 orbits, the planet therefore undergoes accretion for a total of 2000 orbits. Migration is deactivated and the disk is characterized by the parameters $\alpha_{visc} = 10^{-2}$, $h_r = 0.05$. This helps visualize why planets on eccentric orbits accrete at a higher rate than those on cirular orbits, since there is more material in the immediate vicinity of the planet.

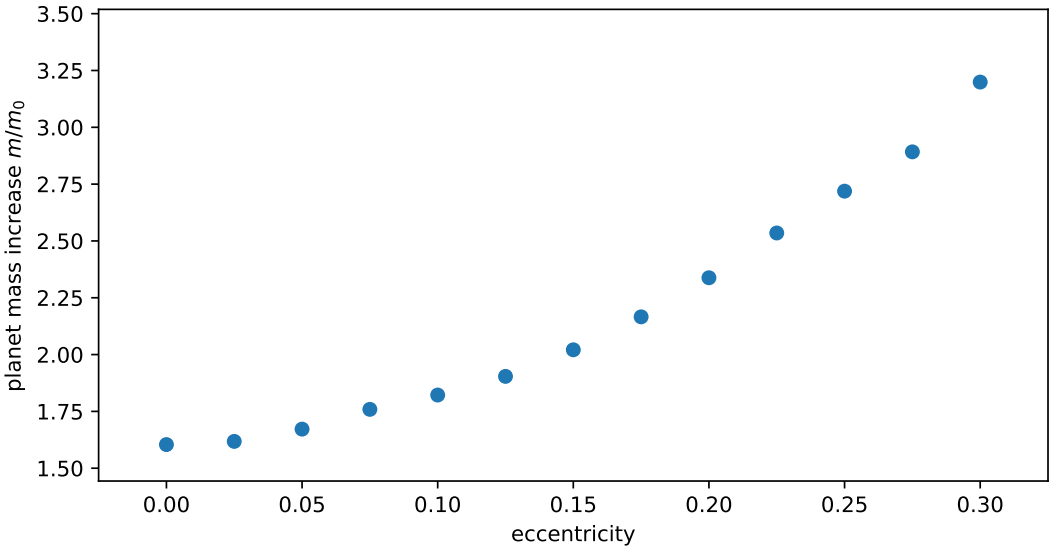

Figure 2.19: Relative planet mass increase as a function of orbit eccentricity at $t = 2500$ orbits. The first 50 of these orbits make up the tapering period, after which $m_0 = 1\ M_{jupiter}$. The planet starts accreting after 500 orbits. Thus, the total accretion time possesses a duration of 2000 orbits. Migration is deactivated and the the disk is characterized by the parameters $\alpha_{visc} = 10^{-2}$, $h_r = 0.05$. Planets on high-eccentricity orbits accrete faster than those on low-eccentricity or cirular orbits.

Influence On Accretion

The relative mass increase m/m_0 after 2000 orbits of accretion is plotted against the orbital eccentricity of the planet in Figure 2.19. Here, the effect of the shallower gap can be seen clearly, as planets on orbits of high eccentricity accrete drastically more gas than those on near-circular or circular orbits.

The evolution of the planet's mass over time is plotted in Figure 2.20a, where we can see how the intially fast mass increase slows down over time as the gap forms. The accretion rate, plotted in Figure 2.20b against time, seems to be converging towards a limiting value.

To further look into this and to find out whether this limiting value is actually the same for the different eccentricity values, a set of simulations is run with an integration time of 50000 orbits. The resulting temporal evolutions of m/m_0 and $\dot{m}$ are displayed in Figure 2.21 on the next page. The limiting value of the accretion rate is determined by the speed at which gas flows back into the gap from the surrounding regions. It is therefore strongly dependent on the gas viscosity.

Additionally, the limiting value seems to possess a dependency on the planet's orbital eccentricity, since even after almost 50000 orbits of acretion, the accretion rates still differ. Higher orbit eccentricities make themselves noticable in accordingly higher accretion rates, which is probably due to the difference in the gas density profile, i.e. the shallower gap.

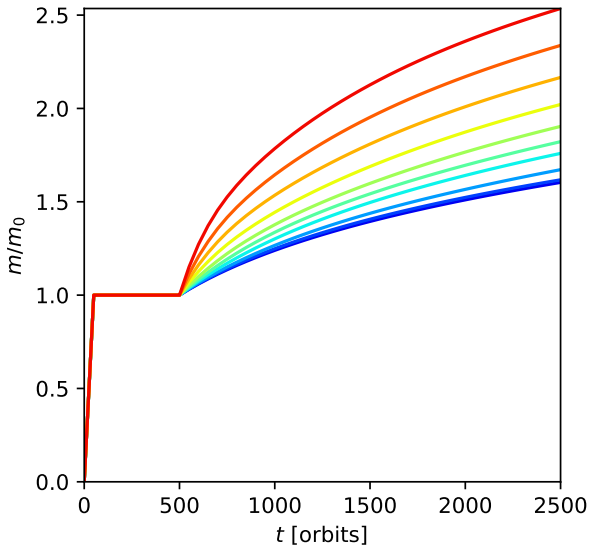

(a) mass increase vs. time and e_0

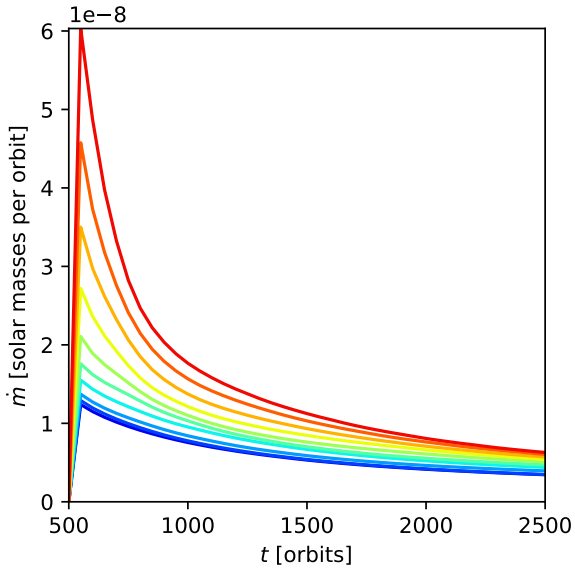

(b) accretion rate vs. time and e_0

Figure 2.20: Influence of the planet eccentricity on the relative mass increase as well as accretion rate during a simulation with an integration time of 2500 orbits. The first 50 of these orbits make up the tapering period, after which $m_0 = 1\ M_{jupiter}$. The planet starts accreting after 500 orbits. Thus, the total duration of accretion is 2000 orbits. Migration is deactivated and the disk is characterized by the parameters $\alpha_{visc} = 10^{-2}$, $h_r = 0.05$. Planets on high-eccentricity accrete gas faster, yet for all values of e_0 the rate of accretion decreases with time as the gap is depleted of the gas. The accretion rate approaches a minimum value determined by the inflow of gas from distant regions into the gap, which depends heavily on the gas viscosity.

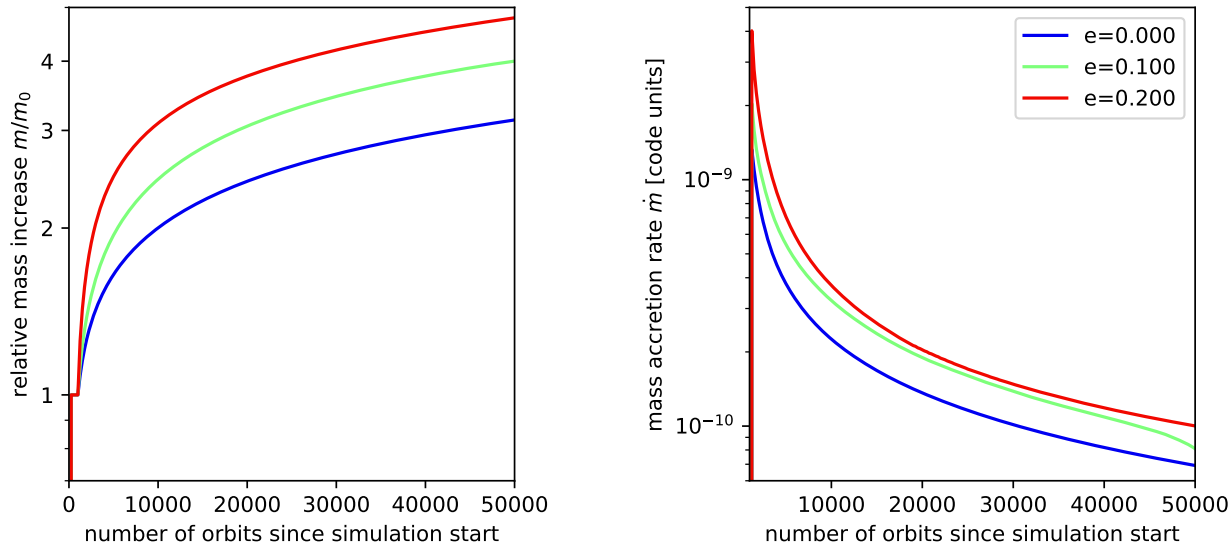

(a) mass increase vs. time and e_0 (b) accretion rate vs. time and e_0

Figure 2.21: Long term evolution: Relative mass increase and accretion rate as a function of time for different orbital eccentricities (plotted logarithmically). The mass of the planet is initialized to $m_0 = 1\ M_{jupiter}$ during a tapering period of 50 orbits, it starts accreting after 1000 orbits. Thus, the total accretion time is 49000 orbits. Migration is deactivated and the disk is characterized by the parameters $\alpha_{visc} = 10^{-2}$, $h_r = 0.05$. The accretion rate falls off over time and approaches a limiting value determined by the speed at which gas from the surrounding regions can flow back into the gap.

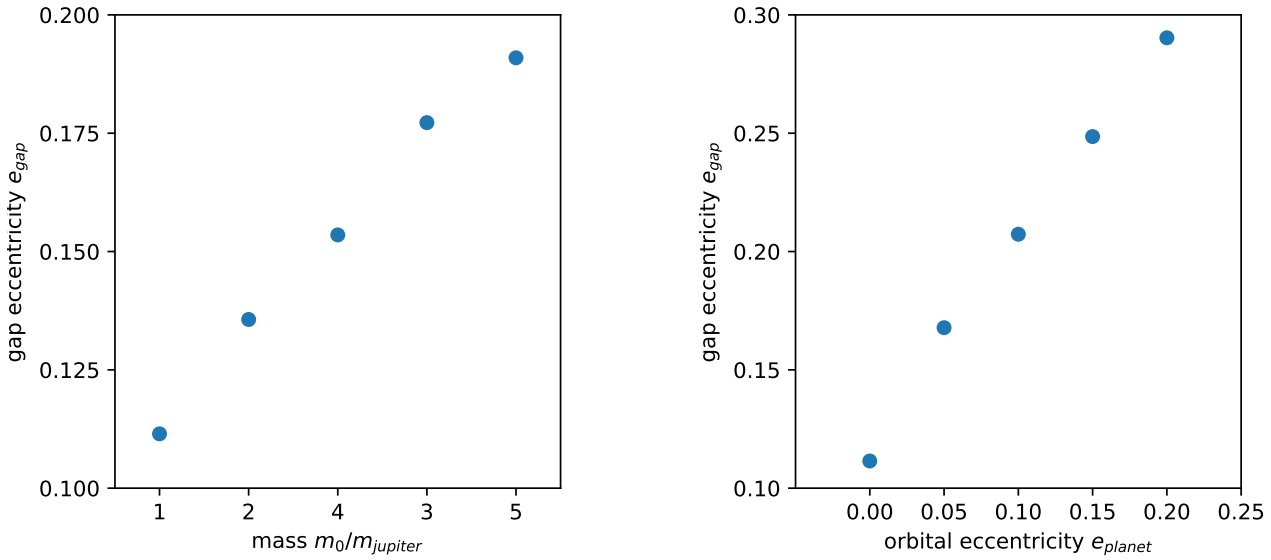

(a) gap eccentricity vs. initial planet mass (b) gap eccentricity vs. initial planet eccentricity

Figure 2.22: Gap eccentricity as a function of the planet's mass and orbital eccentricity (plotted at $t = 2500$ orbits). The first 50 of orbits make up the tapering period and the planet starts accreting after 100 orbits. Thus, the total accretion time has a duration of 2000 orbits. When varying eccentricity, the initial mass of the planet is set to $m_0 = 1\ M_{jupiter}$. When varying the mass, the initial orbital eccentricity is $e_0 = 0$. Migration is deactivated. The disk is characterized by the parameters $\alpha_{visc} = 10^{-2}$, $h_r = 0.05$.

Influence On The Eccentricity Of The Gap

It would be interesting to see how the planetary mass and orbit eccentricity influence the gap eccentricity e_{gap}. To determine an approximation for the value of e_{gap}, each grid cell inside the gap is treated as a free particle on an orbit with eccentricity e_{cell}. The value of e_{cell} can then be calculated for each grid cell individially from the cell's semimajor axis and velocity vector. Afterwards, the average over all cells is taken to obtain an approximation for the eccentricity of the gap as a whole.

To decide whether or not a grid cell belongs to the gap, we use the criterion

$$\Sigma/\Sigma_{unp} \overset{!}{\leq} 0.1$$

This criterion is of course somewhat arbitrary, but it should suffice for getting a first approximation of the value of e_{gap}. Each grid cell in the gap can be attributed a velocity vector $\mathbf{v}$ and a position vector $\mathbf{r}$, which we can get from the output files of the *FARGO2D1D* code. The relationship between the cell's eccentricity e_{cell}, specific angular momentum

$$L_{sp} = \mathbf{r} \times \mathbf{v} \tag{2.13}$$

and semimajor axis a can be expressed as

$$e_{cell} = \sqrt{1 - \frac{L_{sp}^2}{GM_* a}} \tag{2.14}$$

This formula can be derived directly from the law of energy conservation, as has been demonstrated by Bitsch et al. (2013). The eccentricity is determined for each individial grid cell, the average is calculated afterwards. The results can be seen in Figure 2.22, where the gap eccentricity is plotted against the planet mass as well as the planet orbital eccentricity.

It can be seen that the gap eccentricity increases with the planetary mass, as has already been observed by Kley and Dirksen (2006). This could be a one of the mechanisms allowing the formation of planets with $m \gg 5\ m_{jupiter}$, since in the case of a circular gap the planet would experience a near-complete clearing of the gas in its immediate vicinity, which would greatly hinder any further accretion.

Planets on high-eccentricity orbits also lead to higher values of e_{gap}, the eccentricity of the gap can even surpass that of the planet that is creating it. Reasons for this could be spiral density waves created at corotation resonances, as has been discussed in detail be e.g. Hosseinbor et al. (2007).

2.6 Investigating a Migrating Planet

So far, the orbital eccentricity as well as the semimajor (and semiminor) axis have been assumed to be invariant in time to better study the influences of the various disk and planet parameters. The planet was modeled in such a way as not to feel the gravitational influence of the gas particles in the disk. When attempting to accurately model the evolution of a proto-planetary disk, this interaction should not be neglected, since it can lead to changes in the planet's semimajor axis and eccentricity, which then again influence the planet formation processes. We will now look into this.

Multiple simulations are run for various starting masses and eccentricites. In each simulation, a non-accreting planet is placed in orbit around the star. In the beginning, the planet feels only the potential of the star, therefore no migration occurs. The disk does feel the planet though, which leads to the formation of a gap. We wait until a steady gap is reached after 500 orbits and then make two sets of simulations, once with accretion turned on and once with it turned off.

Figure 2.23 and Figure 2.24 show the temporal evolution of the semimajor axis for various eccentricities and masses. In all cases, the planet's semimajor axis experiences a drop-off, the rate of which decreases with time. This behavior has already been reported by e.g. Dürmann and Kley (2015). Immediately after the full interaction of disk and planet is turned on, the rate of decrease in the planet's semimajor axis is the fastest and then slows down. This could be due to a mismatch of the disk structure with a stationary planet in comparison to the evolving case.

It is interesting to see that in the beginning, the steepest semimajor axis drop-off occurs for the planet with $e = 0.2$. This could be explained by the findings of Kanagawa, Tanaka, and Szuszkiewicz (2018), which indicate that the rate of type II migration depends on the depth of the gap around the planet, i.e. shallower gaps lead to faster migration. This might explain why both the planet with $e = 0.1$ and the one with $e = 0.2$ initially undergo a faster migration then the planet on a circular orbit, and for the same reason could explain why the low-mass planet in Figure 2.24 undergoes the fastest migration.

The eccentricity damping over time can be seen in Figure 2.25 and Figure 2.26 on the next page for various masses and eccentricities. The low-mass planets experience a rapid eccentricity damping towards $e = 0$ during the first ~ 100 orbits. This can be explained by the fact that the eccentricity damping originates from Lindblad resonances, which are weaker for more massive planets (see Papaloizou and Terquem, 2001 and Kley and Dirksen, 2006).

The migration behavior appears to proceed very similarly for planets of different eccentricities (see Figure 2.25). The initial eccentricity drop-off is followed by a sequence of decaying oscillations, which can be explained by Kozai resonances (see Kozai, 1962 and Bitsch et al., 2013). Migration is directed only inward, and the planet with $e_0 = 0$ does not experience any relevant changes in its semimajor axis. Studies of planetary migration outwards have been done by e.g. Bitsch et al. (2013).

The overall evolution of both eccentricity and semimajor axis is relatively similar for accreting and non-accreting planets, as has already been observed by Dürmann and Kley (2015). Gas accretion onto the planet does not have a large influence on the overall structure of the disk and gap, therefore it is to be expected that the results do not differ drastically. Still, the migration of accreting planets appears to take a place on slightly longer timescales than that of non-accreting planets. The reason for this is the reduced gas density near of the planet, which leads to weaker torques.

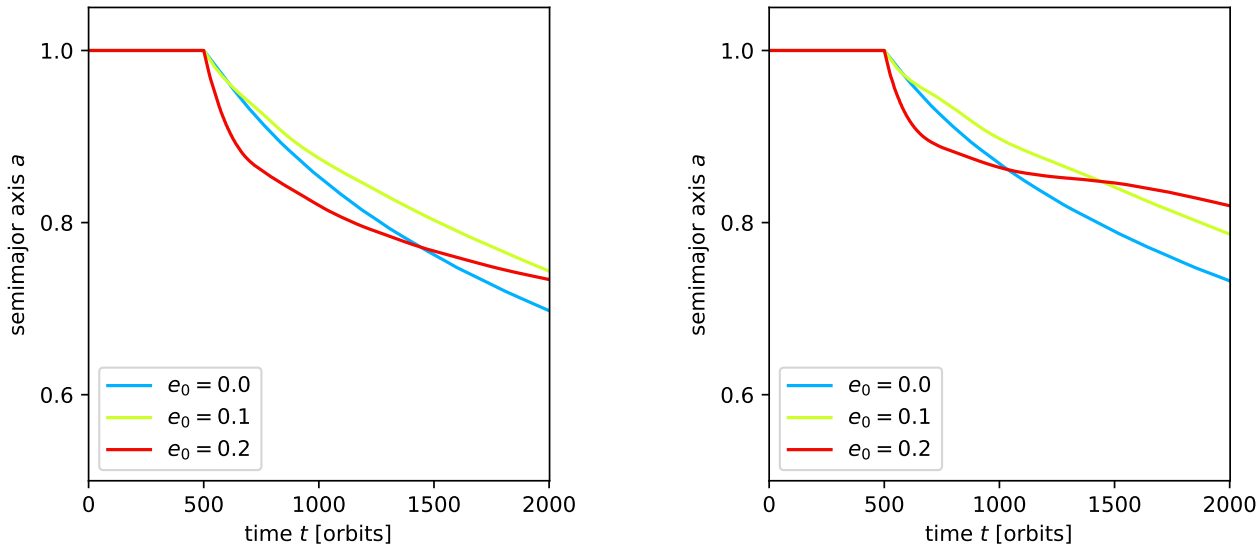

(a) without accretion (b) with accretion

Figure 2.23: Temporal evolution of a migrating planet's semimajor axis for various values of the initial orbital eccentricity during an integration time of 2500 orbits. The first 50 of these orbits make up the tapering period (after which $m_0 = 1\ M_{jupiter}$) and the planet starts accreting after 100 orbits. Thus, the total accretion time possesses a duration of 2000 orbits. The disk is characterized by the parameters $\alpha_{visc} = 10^{-2}$, $h_r = 0.05$.

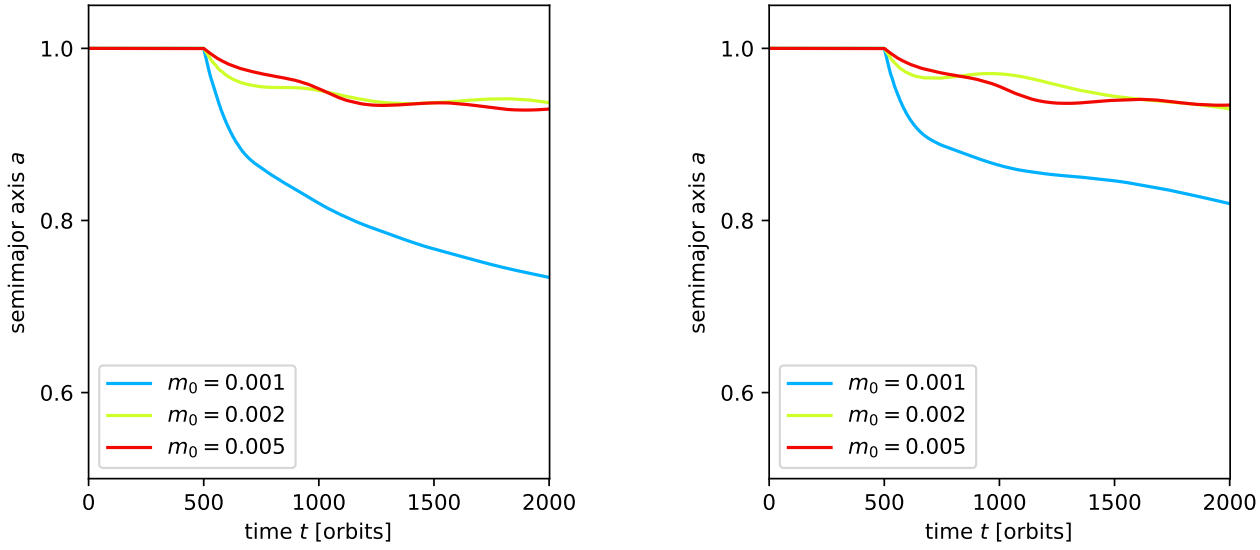

(a) without accretion (b) with accretion

Figure 2.24: Temporal evolution of a migrating planet's semimajor axis for different values of the initial planet mass during an integration time of 2500 orbits. The first 50 of these orbits make up the tapering period and the planet starts accreting after 100 orbits. Thus, the total accretion time possesses a duration of 2000 orbits. The planet is initially put on a circular orbit and the disk is characterized by the parameters $\alpha_{visc} = 10^{-2}$, $h_r = 0.05$. The least massive simulated planet experiences the fastest rate of migration.

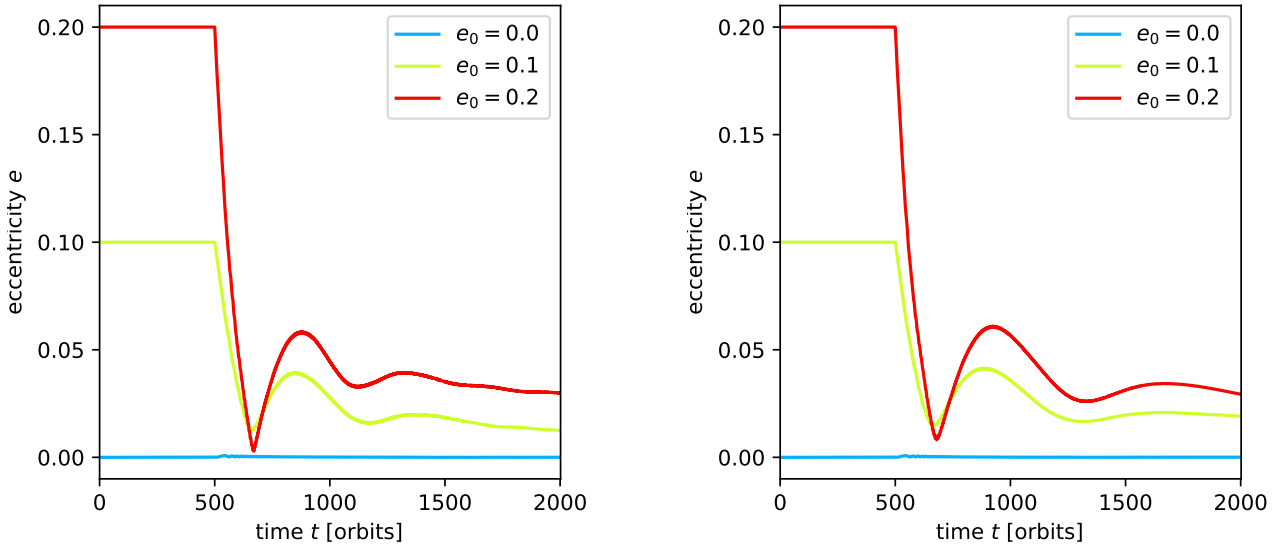

(a) without accretion (b) with accretion

Figure 2.25: Temporal evolution of the orbital eccentricity of a migrating planet for different orbital eccentricites during an integration time of 2500 orbits. The mass of the planet is initialized to $m_0 = 1\ M_{jupiter}$ during a tapering period of 50 orbits. Accretion starts at $t = 100$ orbits. Thus, the planet accretes for a total of 2000 orbits. The disk is characterized by the parameters $\alpha_{visc} = 10^{-2}$, $h_r = 0.05$. The eccentricity damping occurs relatively quickly. The highest rate of damping is observed in the first ~ 100 orbits, afterwards there are oscillations of the eccentricity which decay off over the next ~ 1000 orbits.

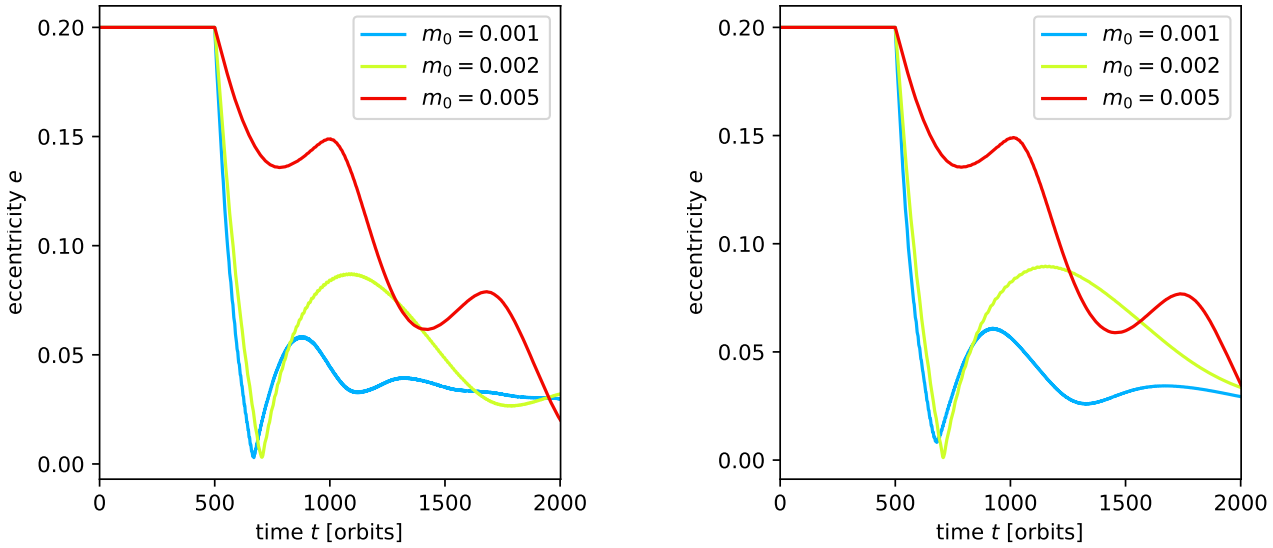

(a) without accretion (b) with accretion

Figure 2.26: Temporal evolution of the orbital eccentricity of a migrating planet for various different initial masses during an integration time of 2500 orbits. The initial eccentricity is set to 0 and the mass of the planet is set during a tapering period of 50 orbits. Accretion starts at $t = 100$ orbits. Thus, the planet accretes for a total of 2000 orbits. The disk is characterized by the parameters $\alpha_{visc} = 10^{-2}$, $h_r = 0.05$. The fastest eccentricity damping happens for low mass planets, the oscillations can be explained by Kozai resonances.

Chapter 3

Results

In this thesis, several studies were done regarding the accretion of gas in proto-planetary disks onto planets on eccentric orbits. The *FARGO2D1D* algorithm was used to simulate a thin, locally isothermal alpha disk. To get familiar with the processes underlying the behavior of the simulated protoplanetary disk, several parameter studies of the gap profile as well as the accretion rate were made, including the gas viscosity parameter, flaring index of the gas density, disk aspect ratio and planet mass. The observations of earlier investigations done by e.g. Crida, Morbidelli, and Masset (2006) and Kley and Dirksen (2006) could be confirmed. Then, the effect of a planet's orbital eccentricity on the surface gas density profile as well as on the accretion rate was investigated.

It could be shown that in the utilized model, a planet's orbital eccentricity greatly influences the gas surface density profile of the gap formed due to exchange processes of angular momentum between disk and planet. Orbits of high eccentricities lead to the formation of much more shallow gaps with accordingly greater radial extension.

This in turn directly influences the amount of gas present in the vicinity of the planet's orbit. To be more precise, the total amount of gas inside the Hill sphere of a planet on an eccentric orbit is larger than it would be for a planet on a circular orbit. Thus, eccentric planets experience a significantly higher rate of gas accretion.

Studies were also made regarding the eccentricity of the gap as a function of the planet mass and orbital eccentricity. It could be observed that both of these values positively influence the eccentricity of the gap. Reasons for this are given in Hosseinbor et al. (2007).

Additionally, the processes of migration and eccentricity damping were investigated. In our model of the disk, the planet experiences a rapid phase of type II inward migration. The rate of change of the semimajor axis depends on the mass as well as the orbital eccentricity of the planet. An explanation for this has been given by Kanagawa, Tanaka, and Szuszkiewicz (2018), who argue that deep gaps lead to slower migration, since the torque exerted on the gap-opening planet depends on the surface density at the bottom of the gap. A deeper gap therefore leads to slower migration, which would be the case for massive planets.

It could be observed that eccentricity damping occurs at a much faster rate for low-mass planets than for ones with larger masses. This can also be explained by the depth of the gap, since deeper gap with less gas lead to weaker Lindblad resonances, which directly affects the migration rate.

Chapter 4

Discussion

The number of discovered exoplanets has grown drastically in recent years. This opens up the opportunity to constrain models of the planetary formation processes using statistical properties extracted from the population of discovered planets. A promising way to link those models with observations is with so-called planet population synthesis, where a population of planets is initialized with randomly distributed parameters. The population is then allowed to evolve over time and can subsequently be compared with observation data to assess the accuracy of the involved models. As such, the most important part of any study using population synthesis is arguably the planet formation model, which takes in a distribution of initial parameters and outputs the properties of the emerging planetary system.

Studies utilizing planet population synthesis this have been conducted by e.g. Ida et al. (2018), Benz et al. (2014) and Mordasini et al. (2012). When formulating a routine which describes the accretion rate of disk material onto a planet, none of these mentioned studies take the planet's orbital eccentricity into account.

As could be shown in this thesis, the orbital eccentricity can play a large role in the accretion process. Thus, when trying to construct an accurate planet formation model, the accretion routine should be modified in such a way as to take these effects into account. It could also be beneficial to do this when running N-body simulations like the ones that have been reported by Bitsch et al. (2019). They also do not take the influence of the orbital eccentricity into account for the formulation of their mass accretion routine. Since planet-planet interaction is a viable mechanism for the creation of highly elliptical orbits, N-body simulations likely lead to a family of bodies orbiting their parent star on orbits with $e \neq 0$. Therefore, these and similar studies could benefit from incorporating an eccentricity dependency into their accretion routine.

The disk model that was used in this thesis is a highly simplified one. While we could show the influence of orbital eccentricities on the rate of accretion in a qualitative way, it would be advantageous to make use of a more sophisticated model, when one really wants to determine an accurate relationship between e and $\dot{m}$. Obvious ways of improvement include the utilization of larger values for the grid resolution and integration time. This thesis also treated the disk as being both locally isothermal and non-flared, as well as ignoring the influence of physical processes like stellar radiation and magneto-hydro-dynamics in the disk, among others. A simulation of protoplanetary disks using a more sophisticated approach could be done to display the relationship between eccentricity and accretion in a more quantitatively accurate manner, which after the fitting of a suitable function would then be able to be used in future studies, improving their results.

Chapter 5

Appendix

5.1 References

[1] ALMA (ESO/NAOJ/NRAO). *ALMA image of the protoplanetary disc around HL Tauri*. URL: https://www.eso.org/public/archives/images/original/eso1436a.tif. (accessed: 11.02.2020).

[2] S. Andrews (Harvard-Smithsonian CfA); B. Saxton (NRAO/AUI/NSF); ALMA (ESO/NAOJ/NRAO). *ALMA image of the disc around the young star TW Hydrae*. URL: https://www.eso.org/public/archives/images/original/eso1611a.tif. (accessed: 11.02.2019).

[3] K. Bailli, S. Charnoz, and E. Pantin. "Trapping planets in an evolving protoplanetary disk: preferred time, locations, and planet mass". In: *Astronomy & Astrophysics* 590 (May 2016), A60. ISSN: 1432-0746. DOI: 10.1051/0004-6361/201528027. URL: http://dx.doi.org/10.1051/0004-6361/201528027.

[4] W. Benz et al. "Planet Population Synthesis". In: *Protostars and Planets VI* (2014). DOI: 10.2458/azu_uapress_9780816531240-ch030. URL: http://dx.doi.org/10.2458/azu_uapress_9780816531240-ch030.

[5] T. Birnstiel, C. P. Dullemond, and F. Brauer. "Gas- and dust evolution in protoplanetary disks". In: *Astronomy & Astrophysics* 513 (Apr. 2010), A79. ISSN: 1432-0746. DOI: 10.1051/0004-6361/200913731. URL: http://dx.doi.org/10.1051/0004-6361/200913731.

[6] B. Bitsch et al. "Formation of planetary systems by pebble accretion and migration: growth of gas giants". In: *Astronomy & Astrophysics* 623 (Mar. 2019), A88. ISSN: 1432-0746. DOI: 10.1051/0004-6361/201834489. URL: http://dx.doi.org/10.1051/0004-6361/201834489.

[7] B. Bitsch et al. "Highly inclined and eccentric massive planets". In: *Astronomy & Astrophysics* 555 (July 2013), A124. ISSN: 1432-0746. DOI: 10.1051/0004-6361/201220310. URL: http://dx.doi.org/10.1051/0004-6361/201220310.

[8] B. Bitsch et al. "Stellar irradiated discs and implications on migration of embedded planets". In: *Astronomy & Astrophysics* 549 (Jan. 2013), A124. ISSN: 1432-0746. DOI: 10.1051/0004-6361/201220159. URL: http://dx.doi.org/10.1051/0004-6361/201220159.

[9] A. Crida, A. Morbidelli, and F. Masset. "On the width and shape of gaps in protoplanetary disks". In: *Icarus* 181.2 (Apr. 2006), pp. 587–604. ISSN: 0019-1035. DOI: 10.1016/j.icarus.2005.10.007. URL: http://dx.doi.org/10.1016/j.icarus.2005.10.007.

[10] C.P. Dullemond and J.D. Monnier. "The Inner Regions of Protoplanetary Disks". In: *Annual Review of Astronomy and Astrophysics* 48.1 (Aug. 2010), pp. 205–239. ISSN: 1545-4282. DOI: 10.1146/annurev-astro-081309-130932. URL: http://dx.doi.org/10.1146/annurev-astro-081309-130932.

[11] Cornelis P. Dullemond et al. "The Disk Substructures at High Angular Resolution Project (DSHARP). VI. Dust Trapping in Thin-ringed Protoplanetary Disks". In: *The Astrophysical Journal* 869.2 (Dec. 2018), p. L46. ISSN: 2041-8213. DOI: 10.3847/2041-8213/aaf742. URL: http://dx.doi.org/10.3847/2041-8213/aaf742.

[12] C. Dürmann and W. Kley. "Migration of massive planets in accreting disks". In: *Astronomy & Astrophysics* 574 (Jan. 2015), A52. ISSN: 1432-0746. DOI: 10.1051/0004-6361/201424837. URL: http://dx.doi.org/10.1051/0004-6361/201424837.

[13] FARGO3D. *2D1D grid*. [Online; accessed January 06, 2020]. URL: http://fargo.in2p3.fr/local/cache-vignettes/L500xH501/gif_1D2Dgrid-352ab.png.

[14] FARGO3D. *What is FARGO2D1D?* URL: http://fargo.in2p3.fr/What-is-FARGO-2D1D. (accessed: 17.01.2020).

[15] Hamilton, D. P. & Burns, J. A. "Orbital stability zones about asteroids. II - The destabilizing effects of eccentric orbits and of solar radiation". In: *Icarus* 96.1 (1992), pp. 43–64. DOI: https://www.sciencedirect.com/science/article/pii/001910359290005R.

[16] A. Pasha Hosseinbor et al. "The formation of an eccentric gap in a gas disc by a planet in an eccentric orbit". In: *Monthly Notices of the Royal Astronomical Society* 378.3 (June 2007), pp. 966–972. ISSN: 1365-2966. DOI: 10.1111/j.1365-2966.2007.11832.x. URL: http://dx.doi.org/10.1111/j.1365-2966.2007.11832.x.

[17] S. Ida et al. "Slowing Down Type II Migration of Gas Giants to Match Observational Data". In: *The Astrophysical Journal* 864.1 (Aug. 2018), p. 77. ISSN: 1538-4357. DOI: 10.3847/1538-4357/aad69c. URL: http://dx.doi.org/10.3847/1538-4357/aad69c.

[18] International Astronomical Union. *Resolution B5: Definition of a Planet in the Solar System*. URL: https://www.iau.org/static/resolutions/Resolution_GA26-5-6.pdf. (accessed: 13.02.2020).

[19] Kazuhiro D. Kanagawa, Hidekazu Tanaka, and Ewa Szuszkiewicz. "Radial Migration of Gap-opening Planets in Protoplanetary Disks. I. The Case of a Single Planet". In: *The Astrophysical Journal* 861.2 (July 2018), p. 140. ISSN: 1538-4357. DOI: 10.3847/1538-4357/aac8d9. URL: http://dx.doi.org/10.3847/1538-4357/aac8d9.

[20] M. Keppler et al. "Discovery of a planetary-mass companion within the gap of the transition disk around PDS 70". In: *Astronomy & Astrophysics* 617 (Sept. 2018), A44. ISSN: 1432-0746. DOI: 10.1051/0004-6361/201832957. URL: http://dx.doi.org/10.1051/0004-6361/201832957.

[21] Kley, W. "Mass flow and accretion through gaps in accretion discs". In: *Monthly Notices of the Royal Astronomical Society* 303.4 (1999), pp. 696–710. DOI: 10.1046/j.1365-8711.1999.02198.x.

[22] W. Kley and G. Dirksen. "Disk eccentricity and embedded planets". In: *Astronomy & Astrophysics* 447.1 (Jan. 2006), pp. 369–377. ISSN: 1432-0746. DOI: 10.1051/0004-6361:20053914. URL: http://dx.doi.org/10.1051/0004-6361:20053914.

[23] Yoshihide Kozai. "Secular perturbations of asteroids with high inclination and eccentricity". In: *Astronomical Journal* 67 (Nov. 1962), pp. 591–598. DOI: 10.1086/108790.

[24] D. N. C. Lin and J. C. B. Papaloizou. "On the Tidal Interaction Between Protostellar Disks and Companions". In: (Jan. 1993). Ed. by Eugene H. Levy and Jonathan I. Lunine, p. 749.

[25] D. N. C. Lin and John Papaloizou. "On the Tidal Interaction between Protoplanets and the Protoplanetary Disk. III. Orbital Migration of Protoplanets". In: *The Astrophysical Journal* 309 (Oct. 1986), p. 846. DOI: 10.1086/164653.

[26] D. Lynden-Bell and J.E. Pringle. "The evolution of viscous discs and the origin of the nebular variables." In: *MNRAS* 168 (Sept. 1974), pp. 603–637. DOI: 10.1093/mnras/168.3.603.

[27] M. Machida et al. "Gas accretion onto a protoplanet and formation of a gas giant planet". In: *Monthly Notices of the Royal Astronomical Society* 405.2 (2010), pp. 1227–1243. DOI: 10.1111/j.1365-2966.2010.16527.x.

[28] Masset, F. "FARGO: A fast Eulerian Transport Algorithm for Differentially Rotating Disks". In: *Astron. Astrophys. Supp. Series* (1999). DOI: 10.1051/aas:2000116.

[29] Soko Matsumura, Ramon Brasser, and Shigeru Ida. "N-body simulations of planet formation via pebble accretion". In: *Astronomy & Astrophysics* 607 (Nov. 2017), A67. ISSN: 1432-0746. DOI: 10.1051/0004-6361/201731155. URL: http://dx.doi.org/10.1051/0004-6361/201731155.

[30] A. Morbidelli. "Accretion Processes". In: (2018). arXiv: 1803.06708 [astro-ph.EP].

[31] A. Morbidelli and S. N. Raymond. "Challenges in planet formation". In: *Journal of Geophysical Research: Planets* 121.10 (Oct. 2016), pp. 1962–1980. ISSN: 2169-9097. DOI: 10.1002/2016je005088. URL: http://dx.doi.org/10.1002/2016JE005088.

[32] C. Mordasini et al. "Characterization of exoplanets from their formation. I. Models of combined planet formation and evolution". In: *Astronomy & Astrophysics* 547, A111 (Nov. 2012), A111. DOI: 10.1051/0004-6361/201118457. arXiv: 1206.6103 [astro-ph.EP].

[33] NASA. *Legacy of NASA's Kepler Space Telescope: More Planets Than Stars*. URL: https://www.nasa.gov/mediacast/legacy-of-nasa-s-kepler-space-telescope-more-planets-than-stars. (accessed: 10.02.2020).

[34] S. -J. Paardekooper and G. Mellema. "Dust flow in gas disks in the presence of embedded planets". In: *Astronomy and Astrophysics* 453.3 (July 2006), pp. 1129–1140. DOI: 10.1051/0004-6361:20054449. arXiv: astro-ph/0603132 [astro-ph].

[35] John C. B. Papaloizou and Caroline Terquem. "Dynamical relaxation and massive extrasolar planets". In: *Monthly Notices of the Royal Astronomical Society* 325.1 (July 2001), pp. 221–230. ISSN: 0035-8711. DOI: 10.1046/j.1365-8711.2001.04386.x. eprint: https://academic.oup.com/mnras/article-pdf/325/1/221/2826930/325-1-221.pdf. URL: https://doi.org/10.1046/j.1365-8711.2001.04386.x.

[36] E. A. Petigura, A. W. Howard, and G. W. Marcy. "Prevalence of Earth-size planets orbiting Sun-like stars". In: *Proceedings of the National Academy of Sciences* 110.48 (Nov. 2013), pp. 19273–19278. ISSN: 1091-6490. DOI: 10.1073/pnas.1319909110. URL: http://dx.doi.org/10.1073/pnas.1319909110.

[37] S. Pfalzner et al. "The formation of the solar system". In: *Physica Scripta* 90.6 (Apr. 2015), p. 068001. ISSN: 1402-4896. DOI: 10.1088/0031-8949/90/6/068001. URL: http://dx.doi.org/10.1088/0031-8949/90/6/068001.

[38] James B. Pollack et al. "Formation of the Giant Planets by Concurrent Accretion of Solids and Gas". In: *Icarus* 124.1 (Nov. 1996), pp. 62–85. DOI: 10.1006/icar.1996.0190.

[39] C. M. T. Robert et al. "Toward a new paradigm for Type II migration". In: *Astronomy & Astrophysics* 617 (Sept. 2018), A98. ISSN: 1432-0746. DOI: 10.1051/0004-6361/201833539. URL: http://dx.doi.org/10.1051/0004-6361/201833539.

[40] M. Schulik et al. "Global 3D radiation-hydrodynamic simulations of gas accretion: Opacity-dependent growth of Saturn-mass planets". In: *Astronomy & Astrophysics* 632 (Dec. 2019), A118. ISSN: 1432-0746. DOI: 10.1051/0004-6361/201935473. URL: http://dx.doi.org/10.1051/0004-6361/201935473.

[41] Kang-Lou Soon et al. "Investigating the gas-to-dust ratio in the protoplanetary disk of HD 142527". In: *Publications of the Astronomical Society of Japan* (Oct. 2019). ISSN: 2053-051X. DOI: 10.1093/pasj/psz112. URL: http://dx.doi.org/10.1093/pasj/psz112.

[42] Daniel Thun, Wilhelm Kley, and Giovanni Picogna. "Circumbinary discs: Numerical and physical behaviour". In: *Astronomy & Astrophysics* 604 (Aug. 2017), A102. ISSN: 1432-0746. DOI: 10.1051/0004-6361/201730666. URL: http://dx.doi.org/10.1051/0004-6361/201730666.

[43] Ward, William R. "Planetary Accretion". In: *Completing the Inventory of the Solar System, Astronomical Society of the Pacific Conference Proceedings* 107 (1996), pp. 337–361. DOI: 1996ASPC..107..337W.

[44] A. Wolszczan and D. A. Frail. "A planetary system around the millisecond pulsar PSR1257 + 12". In: *Nature* 355 (1992), pp. 145–147. DOI: 10.1038/355145a0.

[45] M. M. Woolfson. "The Solar - Origin and Evolution". In: *Quarterly Journal of the Royal Astronomical Society* 34 (Mar. 1993), pp. 1–20.

5.2 Abbreviations

ALMA	Atacama Large Millimeter/submillimeter Array
ESO	European Organisation for Astronomical Research in the Southern Hemisphere
FARGO	Fast Advection in Rotating Gaseous Objects
MPIA	Max Planck Institute for Astronomy
VLT	Very Large Telescope

Declaration

Ich versichere, dass ich diese Arbeit selbstständig verfasst und keine anderen als die angegebenen Quellen und Hilfsmittel benutzt habe.

Heidelberg, den 14. Februar 2020